J. Fluid Mech. (1999), *vol.* 401, *pp.* 85–121. Printed in the United Kingdom

Filtered mass density function for large-eddy simulation of turbulent reacting flows

By F. A. JABERI[1], P. J. COLUCCI[1], S. JAMES[1], P. GIVI[1] AND S. B. POPE[2]

[1] Department of Mechanical and Aerospace Engineering, State University of New York, Buffalo, NY 14260-4400, USA

[2] Sibley School of Mechanical and Aerospace Engineering, Cornell University, Ithaca, NY 14853-1301, USA

(Received 12 November 1997 and in revised form 20 April 1999)

A methodology termed the 'filtered mass density function' (FMDF) is developed and implemented for large-eddy simulation (LES) of variable-density chemically reacting turbulent flows at low Mach numbers. This methodology is based on the extension of the 'filtered density function' (FDF) scheme recently proposed by Colucci *et al.* (1998) for LES of constant-density reacting flows. The FMDF represents the joint probability density function of the subgrid-scale (SGS) scalar quantities and is obtained by solution of its modelled transport equation. In this equation, the effect of chemical reactions appears in a closed form and the influences of SGS mixing and convection are modelled. The stochastic differential equations (SDEs) which yield statistically equivalent results to those of the FMDF transport equation are derived and are solved via a Lagrangian Monte Carlo scheme. The consistency, convergence, and accuracy of the FMDF and the Monte Carlo solution of its equivalent SDEs are assessed. In non-reacting flows, it is shown that the filtered results via the FMDF agree well with those obtained by the 'conventional' LES in which the finite difference solution of the transport equations of these filtered quantities is obtained. The advantage of the FMDF is demonstrated in LES of reacting shear flows with non-premixed reactants. The FMDF results are appraised by comparisons with data generated by direct numerical simulation (DNS) and with experimental measurements. In the absence of a closure for the SGS scalar correlations, the results based on the conventional LES are significantly different from those obtained by DNS. The FMDF results show a closer agreement with DNS. These results also agree favourably with laboratory data of exothermic reacting turbulent shear flows, and portray several of the features observed experimentally.

1. Introduction

Within the past decade, large-eddy simulation (LES) of turbulent reacting flows has been the subject of widespread investigations (McMurtry, Menon & Kerstein 1992; Menon, McMurtry & Kerstein 1993; Gao & O'Brien 1993; Madnia & Givi 1993; Frankel *et al.* 1993; Cook & Riley 1994; Fureby & Lofstrom 1994; Möller, Lundgren & Fureby 1996; Branley & Jones 1997; Cook, Riley & deBruynKops 1997*a*; Cook, Riley & Kosály 1997*b*; Jiménez *et al.* 1997; Mathey & Chollet 1997; Colucci *et al.* 1998; DesJardin & Frankel 1998; Jaberi & James 1998; Réveillon & Vervisch 1998) see Galperin & Orszag (1993); McMurtry, Menon & Kerstein (1993); Libby & Williams

(1994); Fox (1996); Vervisch & Poinsot (1988) for reviews. Amongst these, Colucci *et al.* (1998) recently developed a methodology, termed the 'filtered density function' (FDF) based on an idea originally proposed by Pope (1990). The fundamental property of the FDF is to account for the effects of subgrid-scale (SGS) scalar fluctuations in a probabilistic manner. Colucci *et al.* (1998) developed a transport equation for the FDF in constant-density flows in which the effects of unresolved convection and subgrid mixing are modelled similarly to those in 'conventional' LES, and Reynolds averaging procedures. This transport equation was solved numerically by a Lagrangian Monte Carlo procedure and the results were compared with those obtained by direct numerical simulation (DNS) and by a conventional finite difference LES in which the effects of SGS scalar fluctuations are ignored (LES-FD). It was shown that in non-reacting flows, the first two SGS moments of the FDF as obtained by the Monte Carlo solution are close to those obtained by LES-FD. The advantage of the FDF was demonstrated in reacting flows in which its results were shown to deviate significantly from those obtained by LES-FD but compare favourably with DNS data.

The encouraging results generated by FDF warrant its extension and application to more complex flows. Further assessment of its predictive capability is also in order. The primary objective in this work is to extend the FDF methodology for treatment of variable-density reacting flows so that exothermic chemical reactions can be simulated. For that, we introduce the 'filtered mass density function' (FMDF). With the definition of the FMDF, the mathematical framework for its implementation in LES of reacting flows is established. A new computational scheme is also developed for the solution of the FMDF transport equation. The results obtained by FMDF are scrutinized by comparisons with DNS and laboratory data in several turbulent reacting flows with non-premixed reactants. The FMDF deals only with scalar quantities; the hydrodynamic field is obtained via conventional LES. Also, the formulation is based on the assumption of low Mach number. This allows consideration of exothermicity and variable-density effects, but the method cannot be used for LES of very high-speed flows (Drummond 1991).

2. Governing equations

In a compressible flow undergoing chemical reaction, the primary transport variables are the density ρ, the velocity vector u_i, $i = 1, 2, 3$ along the x_i-direction, the total specific enthalpy h, the pressure p, and the species mass fractions Y_α ($\alpha = 1, 2, \ldots, N_s$). The conservation equations governing these variables are the continuity, momentum, enthalpy (energy) and species mass fraction equations, along with an equation of state (Williams 1985)

$$\frac{\partial \rho}{\partial t} + \frac{\partial \rho u_i}{\partial x_i} = 0, \tag{1}$$

$$\frac{\partial \rho u_j}{\partial t} + \frac{\partial \rho u_i u_j}{\partial x_i} = -\frac{\partial p}{\partial x_j} + \frac{\partial \tau_{ij}}{\partial x_i}, \tag{2}$$

$$\frac{\partial \rho \phi_\alpha}{\partial t} + \frac{\partial \rho u_i \phi_\alpha}{\partial x_i} = -\frac{\partial J_i^\alpha}{\partial x_i} + \rho S_\alpha, \quad \alpha = 1, 2, \ldots, \ \sigma = N_s + 1, \tag{3}$$

$$p = \rho R^0 T \sum_{\alpha=1}^{N_s} Y_\alpha / \mathscr{M}_\alpha = \rho \mathscr{R} T, \tag{4}$$

where t represents time, R^0 is the universal gas constant and $\mathscr{M}_\alpha$ denotes the molecular weight of species α. Equation (4) effectively defines the mixture gas constant $\mathscr{R}$. Equation (3) represents the transport of the species' mass fractions and enthalpy in a common form with

$$\phi_\alpha \equiv Y_\alpha,\ \alpha = 1, 2, \ldots, N_s, \quad \phi_\sigma \equiv h = \sum_{\alpha=1}^{N_s} h_\alpha \phi_\alpha, \tag{5}$$

with

$$h_\alpha = h_\alpha^0 + \int_{T_0}^{T} c_{p_\alpha}(T')\,\mathrm{d}T', \tag{6}$$

where T denotes the temperature, T_0 is the reference temperature and h_α^0 and c_{p_α} denote the enthalpy at T_0, and the specific heat of species α at constant pressure, respectively. At low Mach numbers and heat release rates, by neglecting the viscous dissipation and thermal radiation the source terms in the enthalpy equation

$$S_\sigma = \frac{1}{\rho}\frac{\mathrm{D}p}{\mathrm{D}t} \approx \frac{1}{\rho}\frac{\partial p}{\partial t}$$

can be assumed to be negligible. Thus, the chemical source terms ($S_\alpha = S_\alpha(\boldsymbol{\phi}), \boldsymbol{\phi} = [Y_1, Y_2, \ldots, Y_{N_s}, h]$) are functions of the composition variables ($\boldsymbol{\phi}$). For a Newtonian fluid with zero bulk viscosity and Fickian diffusion, the viscous stress tensor τ_{ij}, mass and heat flux ($J_i^\alpha,\ \alpha = 1, 2, \ldots, \sigma$) are given by

$$\tau_{ij} = \mu\left(\frac{\partial u_i}{\partial x_j} + \frac{\partial u_j}{\partial x_i} - \frac{2}{3}\frac{\partial u_k}{\partial x_k}\delta_{ij}\right), \tag{7}$$

$$J_i^\alpha = -\gamma\frac{\partial \phi_\alpha}{\partial x_i}, \tag{8}$$

where μ is the dynamic viscosity and $\gamma = \rho\Gamma$ denotes the thermal and the mass molecular diffusivity coefficients. Both μ and γ are assumed constant and the Lewis number is assumed to be unity. In reactive flows, molecular processes are much more complicated than portrayed by (8). But since the molecular diffusion is typically less important than the SGS diffusion (to be defined below), this simple model is adopted with the justifications and caveats given by Pope (1985) and Bilger (1982).

Large-eddy simulation involves the use of the spatial filtering operation (Aldama 1990)

$$\langle f(\boldsymbol{x}, t)\rangle_\ell = \int_{-\infty}^{+\infty} f(\boldsymbol{x}', t)\mathscr{G}(\boldsymbol{x}', \boldsymbol{x})\,\mathrm{d}\boldsymbol{x}', \tag{9}$$

where $\mathscr{G}$ denotes the filter function of width Δ_G, $\langle f(\boldsymbol{x}, t)\rangle_\ell$ represents the filtered value of the transport variable $f(\boldsymbol{x}, t)$, and $f' = f - \langle f\rangle_\ell$ denotes the fluctuations of f from the filtered value. In variable-density flows it is convenient to consider the Favre-filtered quantity $\langle f(\boldsymbol{x}, t)\rangle_L = \langle \rho f\rangle_\ell / \langle \rho\rangle_\ell$ and the fluctuation $f'' = f - \langle f\rangle_L$. We consider spatially and temporally invariant and localized filter functions, $\mathscr{G}(\boldsymbol{x}', \boldsymbol{x}) \equiv G(\boldsymbol{x}' - \boldsymbol{x})$ with the properties (Aldama 1990) $G(\boldsymbol{x}) = G(-\boldsymbol{x})$, and $\int_{-\infty}^{\infty} G(\boldsymbol{x})\,\mathrm{d}\boldsymbol{x} = 1$. Moreover, we only consider 'positive' filter functions as defined by Vreman, Geurts & Kuerten (1994) for which all the moments $\int_{-\infty}^{\infty} x^m G(x)\,\mathrm{d}x$ exist for $m \geqslant 0$. The application of the filtering operation to the transport equations yields

$$\frac{\partial \langle \rho\rangle_\ell}{\partial t} + \frac{\partial \langle \rho\rangle_\ell \langle u_i\rangle_L}{\partial x_i} = 0, \tag{10}$$

$$\frac{\partial \langle\rho\rangle_\ell \langle u_j\rangle_L}{\partial t} + \frac{\partial \langle\rho\rangle_\ell \langle u_i\rangle_L \langle u_j\rangle_L}{\partial x_i} = -\frac{\partial \langle p\rangle_\ell}{\partial x_j} + \frac{\partial \langle\tau_{ij}\rangle_\ell}{\partial x_i} - \frac{\partial T_{ij}}{\partial x_i}, \tag{11}$$

$$\frac{\partial \langle\rho\rangle_\ell \langle\phi_\alpha\rangle_L}{\partial t} + \frac{\partial \langle\rho\rangle_\ell \langle u_i\rangle_L \langle\phi_\alpha\rangle_L}{\partial x_i} = -\frac{\partial \langle J_i^\alpha\rangle_\ell}{\partial x_i} - \frac{\partial M_i^\alpha}{\partial x_i} + \langle\rho S_\alpha\rangle_\ell, \quad \alpha = 1, 2, \ldots, \sigma, \tag{12}$$

where $T_{ij} = \langle\rho\rangle_\ell(\langle u_i u_j\rangle_L - \langle u_i\rangle_L\langle u_j\rangle_L)$ and $M_i^\alpha = \langle\rho\rangle_\ell(\langle u_i\phi_\alpha\rangle_L - \langle u_i\rangle_L\langle\phi_\alpha\rangle_L)$ denote the subgrid stress and the subgrid mass flux, respectively. The filtered reaction source terms are denoted by $\langle\rho S_\alpha\rangle_\ell = \langle\rho\rangle_\ell\langle S_\alpha\rangle_L$ ($\alpha = 1, 2, \ldots, N_s$).

2.1. *Modelling of hydrodynamic SGS quantities*

In LES of non-reacting flows the closure problem is associated with T_{ij} and M_i^α (Erlebacher *et al.* 1992; Salvetti & Banerjee 1995). In reacting flows, an additional model is required for the filtered reaction rate $\langle S_\alpha\rangle_L$. This is the subject of the probability formulation as described in the next section. For T_{ij}, the variable-density form of the model used in our previous work (Colucci *et al.* 1998) is considered:

$$T_{ij} = -2C_R\langle\rho\rangle_\ell \Delta_G \mathscr{E}^{1/2}\left(\langle\mathscr{S}_{ij}\rangle_L - \tfrac{1}{3}\langle\mathscr{S}_{kk}\rangle_L\delta_{ij}\right) + \tfrac{2}{3}C_I\langle\rho\rangle_\ell\mathscr{E}\delta_{ij}, \tag{13}$$

where $\langle\mathscr{S}_{ij}\rangle_L$ is the resolved strain rate tensor, $\mathscr{E} = |\langle u_i^*\rangle_L\langle u_i^*\rangle_L - \langle\langle u_i^*\rangle_L\rangle_{\ell'}\langle\langle u_i^*\rangle_L\rangle_{\ell'}|$, $u_i^* = u_i - \mathscr{U}_i$ and $\mathscr{U}_i$ is a reference velocity in the x_i-direction. The subscript ℓ' denotes the filter at the secondary level of size $\Delta_{G'} > \Delta_G$. This model is essentially a modified version of that proposed by Bardina, Ferziger & Reynolds (1983), which utilize equal sizes for the grid and secondary filters. We refer to this as the modified kinetic energy viscosity (MKEV) closure. Accordingly, the subgrid eddy viscosity is expressed as $\nu_t = C_R\Delta_G\mathscr{E}^{1/2}$. A similar diffusivity model is used for the closure of the subgrid mass flux (Eidson 1985)

$$M_i^\alpha = -\gamma_t\frac{\partial\langle\phi_\alpha\rangle_L}{\partial x_i}, \tag{14}$$

where $\gamma_t = \langle\rho\rangle_\ell\Gamma_t$, $\Gamma_t = \nu_t/Sc_t$, and Sc_t is the subgrid Schmidt number, assumed to be constant and equal to the subgrid Prandtl number. It must be indicated here that this model is not used directly in the FMDF but the modelled FMDF transport equation is constructed to be consistent with it as discussed below.

3. The filtered mass density function (FMDF)

Let $\boldsymbol{\phi}(\boldsymbol{x}, t)$ denote the scalar array. We define the 'filtered mass density function' (FMDF), denoted by F_L, as

$$F_L(\boldsymbol{\psi}; \boldsymbol{x}, t) \equiv \int_{-\infty}^{+\infty}\rho(\boldsymbol{x}', t)\zeta\left[\boldsymbol{\psi}, \boldsymbol{\phi}(\boldsymbol{x}', t)\right] G(\boldsymbol{x}' - \boldsymbol{x})\,\mathrm{d}\boldsymbol{x}', \tag{15}$$

$$\zeta\left[\boldsymbol{\psi}, \boldsymbol{\phi}(\boldsymbol{x}, t)\right] = \delta[\boldsymbol{\psi} - \boldsymbol{\phi}(\boldsymbol{x}, t)] \equiv \prod_{\alpha=1}^{\sigma}\delta[\psi_\alpha - \phi_\alpha(\boldsymbol{x}, t)], \tag{16}$$

where δ denotes the delta function and $\boldsymbol{\psi}$ denotes the composition domain of the scalar array. The term $\zeta[\boldsymbol{\phi}, \boldsymbol{\psi}(\boldsymbol{x}, t)]$ is the 'fine-grained' density (O'Brien 1980; Pope 1985), and (15) implies that the FMDF is the *mass-weighted spatially filtered* value of the fine-grained density. The integral property of the FMDF is such that

$$\int_{-\infty}^{+\infty}F_L(\boldsymbol{\psi}; \boldsymbol{x}, t)\,\mathrm{d}\boldsymbol{\psi} = \int_{-\infty}^{+\infty}\rho(\boldsymbol{x}', t)G(\boldsymbol{x}' - \boldsymbol{x})\,\mathrm{d}\boldsymbol{x}' = \langle\rho(\boldsymbol{x}, t)\rangle_\ell. \tag{17}$$

For further developments, the mass-weighted conditional filtered mean of the variable $Q(\boldsymbol{x},t)$ is defined as

$$\langle Q(\boldsymbol{x},t)|\boldsymbol{\psi}\rangle_\ell \equiv \frac{\displaystyle\int_{-\infty}^{+\infty} \rho(\boldsymbol{x}',t)Q(\boldsymbol{x}',t)\zeta\left[\boldsymbol{\psi},\boldsymbol{\phi}(\boldsymbol{x}',t)\right] G(\boldsymbol{x}'-\boldsymbol{x})\,\mathrm{d}\boldsymbol{x}'}{F_L(\boldsymbol{\psi};\boldsymbol{x},t)}. \tag{18}$$

Equation (18) implies

$$\text{(i)}\quad \text{for } Q(\boldsymbol{x},t)=c,\quad \langle Q(\boldsymbol{x},t)|\boldsymbol{\psi}\rangle_\ell = c, \tag{19}$$

$$\text{(ii)}\quad \text{for } Q(\boldsymbol{x},t)\equiv \hat{Q}(\boldsymbol{\phi}(\boldsymbol{x},t)),\quad \langle Q(\boldsymbol{x},t)|\boldsymbol{\psi}\rangle_\ell = \hat{Q}(\boldsymbol{\psi}), \tag{20}$$

$$\text{(iii)}\quad \text{integral property}: \int_{-\infty}^{+\infty} \langle Q(\boldsymbol{x},t)|\boldsymbol{\psi}\rangle_\ell F_L(\boldsymbol{\psi};\boldsymbol{x},t)\,\mathrm{d}\boldsymbol{\psi} = \langle\rho(\boldsymbol{x},t)\rangle_\ell\langle Q(\boldsymbol{x},t)\rangle_L, \tag{21}$$

where c is a constant, and $\hat{Q}(\boldsymbol{\phi}(\boldsymbol{x},t))\equiv Q(\boldsymbol{x},t)$ denotes the case where the variable Q can be completely described by the compositional variable $\boldsymbol{\phi}(\boldsymbol{x},t)\equiv[\phi_1,\phi_2,\ldots,\phi_\sigma]$. From these properties, it follows that the filtered value of any function of the scalar variables (such as $\rho\equiv\hat{\rho}[\boldsymbol{\phi}(\boldsymbol{x},t)]$ and $S_\alpha\equiv\hat{S}_\alpha[\boldsymbol{\phi}(\boldsymbol{x},t)]$) is obtained by integration over the composition space.

By applying the method developed by Lundgren (1969), Pope (1976) and O'Brien (1980) to (3), a transport equation is obtained for the fine-grained density (Colucci *et al.* 1998). The transport equation for $F_L(\boldsymbol{\psi};\boldsymbol{x},t)$ is obtained by multiplying the equation for the fine-grained density by the filter function $G(\boldsymbol{x}'-\boldsymbol{x})$ and integrating over $\boldsymbol{x}'$-space. The final result after some algebraic manipulation is

$$\frac{\partial F_L(\boldsymbol{\psi};\boldsymbol{x},t)}{\partial t} + \frac{\partial[\langle u_i(\boldsymbol{x},t)|\boldsymbol{\psi}\rangle_\ell F_L(\boldsymbol{\psi};\boldsymbol{x},t)]}{\partial x_i} = \frac{\partial}{\partial\psi_\alpha}\left[\left\langle\frac{1}{\hat{\rho}(\boldsymbol{\phi})}\frac{\partial J_i^\alpha}{\partial x_i}|\boldsymbol{\psi}\right\rangle_\ell F_L(\boldsymbol{\psi};\boldsymbol{x},t)\right] - \frac{\partial[\hat{S}_\alpha(\boldsymbol{\psi})F_L(\boldsymbol{\psi};\boldsymbol{x},t)]}{\partial\psi_\alpha}. \tag{22}$$

This is an exact transport equation for the FMDF. The last term on the right-hand side of this equation is due to chemical reaction and is in a closed form. The unclosed nature of SGS convection and mixing is indicated by the conditional filtered values. These terms are modelled in a manner consistent with Reynolds averaging and conventional LES in non-reacting flows. The convection term is decomposed via

$$\langle u_i|\boldsymbol{\psi}\rangle_\ell F_L = \langle u_i\rangle_L F_L + [\langle u_i|\boldsymbol{\psi}\rangle_\ell - \langle u_i\rangle_L]F_L, \tag{23}$$

where the second term on the right-hand side denotes the influence of SGS convective flux. This term is modelled as

$$[\langle u_i|\boldsymbol{\psi}\rangle_\ell - \langle u_i\rangle_L]F_L = -\gamma_t\frac{\partial(F_L/\langle\rho\rangle_\ell)}{\partial x_i}. \tag{24}$$

The advantage of the decomposition (23) and the subsequent model (24) is that they yield results similar to that in conventional LES (Germano 1992; Gao & O'Brien 1993; Salvetti & Banerjee 1995). The first Favre moments corresponding to (23) and (24) are

$$\langle u_i\phi_\alpha\rangle_L = \langle u_i\rangle_L\langle\phi_\alpha\rangle_L + [\langle u_i\phi_\alpha\rangle_L - \langle u_i\rangle_L\langle\phi_\alpha\rangle_L], \tag{25}$$

$$\langle\rho\rangle_\ell[\langle u_i\phi_\alpha\rangle_L - \langle u_i\rangle_L\langle\phi_\alpha\rangle_L] = -\gamma_t\frac{\partial\langle\phi_\alpha\rangle_L}{\partial x_i}. \tag{26}$$

The term within square brackets in (25) is the generalized scalar flux. This makes (26) identical to (14). The closure adopted for the SGS mixing is based on the linear mean-square estimation (LMSE) model (O'Brien 1980; Dopazo & O'Brien 1976), also known as the IEM (interaction by exchange with the mean) (Borghi 1988)

$$\frac{\partial}{\partial \psi_\alpha}\left[\left\langle -\frac{1}{\hat{\rho}}\frac{\partial}{\partial x_i}\left(\gamma\frac{\partial \phi_\alpha}{\partial x_i}\right)|\boldsymbol{\psi}\right\rangle_\ell F_L\right] = \frac{\partial}{\partial x_i}\left(\gamma\frac{\partial(F_L/\hat{\rho})}{\partial x_i}\right) + \frac{\partial}{\partial \psi_\alpha}\left[\Omega_m(\psi_\alpha - \langle\phi_\alpha\rangle_L)F_L\right], \tag{27}$$

where $\Omega_m(\boldsymbol{x}, t)$ is the 'frequency of mixing within the subgrid' which is not known *a priori*. This frequency is modelled as $\Omega_m = C_\Omega(\gamma + \gamma_t)/(\langle\rho\rangle_\ell \Delta_G^2)$. For the first term on the right-hand side of (27) an additional minor assumption is made:

$$\frac{\partial}{\partial x_i}\left(\gamma\frac{\partial(F_L/\hat{\rho})}{\partial x_i}\right) \approx \frac{\partial}{\partial x_i}\left(\gamma\frac{\partial(F_L/\langle\rho\rangle_\ell)}{\partial x_i}\right). \tag{28}$$

This assumption is not necessary for the treatment of FMDF and is only adopted to establish consistency between the FMDF and the conventional LES. With these approximations, the modelled FMDF transport equation is

$$\frac{\partial F_L}{\partial t} + \frac{\partial[\langle u_i\rangle_L F_L]}{\partial x_i} = \frac{\partial}{\partial x_i}\left[(\gamma + \gamma_t)\frac{\partial(F_L/\langle\rho\rangle_\ell)}{\partial x_i}\right] + \frac{\partial}{\partial \psi_\alpha}\left[\Omega_m(\psi_\alpha - \langle\phi_\alpha\rangle_L)F_L\right] - \frac{\partial[\hat{S}_\alpha F_L]}{\partial \psi_\alpha}. \tag{29}$$

This equation may be integrated to obtain transport equations for the SGS moments. The equations for the first subgrid Favre moment, $\langle\phi_\alpha\rangle_L$, and the generalized subgrid variance, $\sigma_\alpha^2 = \langle\phi_{(\alpha)}^2\rangle_L - \langle\phi_{(\alpha)}\rangle_L^2$ are

$$\frac{\partial(\langle\rho\rangle_\ell\langle\phi_\alpha\rangle_L)}{\partial t} + \frac{\partial(\langle\rho\rangle_\ell\langle u_i\rangle_L\langle\phi_\alpha\rangle_L)}{\partial x_i} = \frac{\partial}{\partial x_i}\left[(\gamma + \gamma_t)\frac{\partial\langle\phi_\alpha\rangle_L}{\partial x_i}\right] + \langle\rho\rangle_\ell\langle S_\alpha\rangle_L, \tag{30}$$

$$\frac{\partial(\langle\rho\rangle_\ell\sigma_\alpha^2)}{\partial t} + \frac{\partial(\langle\rho\rangle_\ell\langle u_i\rangle_L\sigma_\alpha^2)}{\partial x_i} = \frac{\partial}{\partial x_i}\left[(\gamma + \gamma_t)\frac{\partial\sigma_\alpha^2}{\partial x_i}\right] + 2(\gamma + \gamma_t)\left[\frac{\partial\langle\phi_{(\alpha)}\rangle_L}{\partial x_i}\frac{\partial\langle\phi_{(\alpha)}\rangle_L}{\partial x_i}\right] - 2\Omega_m\langle\rho\rangle_\ell\sigma_\alpha^2 + 2\langle\rho\rangle_\ell\left(\langle\phi_{(\alpha)}S_{(\alpha)}\rangle_L - \langle\phi_{(\alpha)}\rangle_L\langle S_{(\alpha)}\rangle_L\right), \tag{31}$$

where the subscripts in parentheses are excluded from the summation convention. These equations are identical to those which can be derived by filtering (3) directly, and employing consistent closures for the subgrid flux and the dissipation. In such direct moment closure formulation, however, the terms involving $\langle S_\alpha\rangle_L$ remain unclosed.

4. Monte Carlo solution of the FMDF

The Lagrangian Monte Carlo procedure (Pope 1985) is employed for the solution of (29). In this procedure, each of the Monte Carlo elements (particles) obeys certain equations which govern their transport. These particles undergo motion in physical space by convection due to the filtered mean flow velocity and diffusion due to molecular and subgrid diffusivities. The compositional values of each particle are changed due to mixing and reaction. The spatial transport of the FMDF is represented by the general diffusion process governed by the stochastic differential equation (SDE) (Risken 1989; Gardiner 1990)

$$\mathrm{d}X_i(t) = D_i(\boldsymbol{X}(t), t)\,\mathrm{d}t + E(\boldsymbol{X}(t), t)\mathrm{d}W_i(t), \tag{32}$$

where X_i is the Lagrangian position of a stochastic particle, D_i and E are the 'drift' and 'diffusion' coefficients, respectively, and W_i denotes the Wiener process (Karlin & Taylor 1981). The drift and diffusion coefficients are obtained by comparing the Fokker–Planck equation corresponding to (32) with the spatial derivative terms in the FMDF transport equation (29),

$$E \equiv \sqrt{2(\gamma + \gamma_t)/\langle\rho\rangle_\ell}, \quad D_i \equiv \langle u_i\rangle_L + \frac{1}{\langle\rho\rangle_\ell}\frac{\partial(\gamma + \gamma_t)}{\partial x_i}. \tag{33}$$

The subgrid mixing and reaction terms are implemented by altering the compositional makeup of the particles

$$\frac{\mathrm{d}\phi_\alpha^+}{\mathrm{d}t} = -\Omega_m(\phi_\alpha^+ - \langle\phi_\alpha\rangle_L) + \hat{S}_\alpha(\boldsymbol{\phi}^+), \tag{34}$$

where $\phi_\alpha^+ = \phi_\alpha(\boldsymbol{X}(t), t)$ denotes the scalar value of the particle with the Lagrangian position vector X_i. The solutions of (32) and (34) yield the same statistics as those obtained directly from the solution of the FMDF transport equation according to the principle of *equivalent systems* (Pope 1985, 1994).

4.1. *Numerical solution procedure*

A new computational algorithm is developed for the solution of the FMDF. While the algorithm is similar to that used in PDF methods (Pope 1985), it is not exactly the same. Therefore, a detailed description is provided.

The complete numerical solution of the equations governing the resolved field is based on a hybrid scheme in which the hydrodynamic Favre-filtered equations (10) and (11) are integrated by a finite difference method and the filtered scalar field is simulated by the Monte Carlo solution of the FMDF transport equation. The LES of the hydrodynamic variables, which also determines the subgrid viscosity and scalar diffusion coefficients, is conducted with the 'compact parameter' scheme of Carpenter (1990). This scheme is based on a hyperbolic solver which considers a fully compressible flow. Here, the simulations are conducted at a low Mach number to minimize compressibility effects. All the finite difference operations are conducted on a fixed and uniform grid. Thus, the filtered values of the hydrodynamic variables are determined on these grid points. The transfer of information from these points to the location of the Monte Carlo particles (described below) is conducted via interpolation. Both fourth-order and second-order (bilinear) interpolations schemes were considered, but no significant differences in filtered quantities were observed. The results presented below utilize fourth- and second-order interpolation for two-dimensional and three-dimensional simulations, respectively.

The FMDF is represented by an ensemble of Monte Carlo particles, each with a set of scalars $\phi_\alpha^{(n)}(t) = \phi_\alpha(\boldsymbol{X}^{(n)}(t), t)$ and Lagrangian position vector $\boldsymbol{X}^{(n)}$. A splitting operation is employed in which transport in the physical and compositional domains is treated separately. The simplest means of simulating (32) is via the Euler–Maruyamma approximation (Kloeden & Platen 1995): $X_i^{(n)}(t_{k+1}) = X_i^{(n)}(t_k) + D_i^{(n)}(t_k)\Delta t + E^{(n)}(t_k)(\Delta t)^{1/2}\xi_i^{(n)}(t_k)$, where $\Delta t = t_{k+1} - t_k$ is the computational time increment between two consecutive discretized time levels, $D_i^{(n)}(t) = D_i(\boldsymbol{X}^{(n)}(t), t)$, $E^{(n)}(t) = E(\boldsymbol{X}^{(n)}(t), t)$ and $\xi_i^{(n)}$ is a random variable with the standard Gaussian PDF. The coefficients D_i and E require the input of the filtered mean velocity and the diffusivity (molecular and subgrid). These are provided by finite difference solution of (10) and (11).

The compositional values are subject to change due to SGS mixing and chemical

reaction. Equation (34) may be integrated numerically to simulate these effects simultaneously. Alternatively, this equation is treated in a split manner. This provides an analytical expression for the subgrid mixing. Subsequently, the influence of chemical reaction is determined by evaluating the fine-grained reaction rates $S_\alpha^{(n)} = \hat{S}_\alpha(\boldsymbol{\phi}^{(n)})$ and modifying the composition. The mixing model requires the Favre-filtered scalar values. These and other higher moments of the FMDF at a given point are estimated by consideration of particles within a volume centred at the point of interest. Effectively, this finite volume constitutes an 'ensemble domain' characterized by the length scale Δ_E (not to be confused with Δ_G) in which the FMDF is discretely represented. A box of size Δ_E is used to construct the statistics at the finite difference nodes. These are then interpolated to the particle positions. Since the SGS mixing model only requires the input of the filtered scalar values, and not their derivative, this volume averaging is sufficient. From a numerical standpoint, specification of the size of the ensemble domain is an important issue. Ideally, it is desired to obtain the statistics from the Monte Carlo solution when the size of sample domain is infinitely small ($\Delta_E \to 0$) and the number of particles within this domain is infinitely large. With a finite number of particles, if Δ_E is small there may not be enough particles to construct reliable statistics. A larger ensemble domain decreases the statistical error, but increases the spatial error which manifests itself in artificially diffused statistical results. This compromise between the statistical accuracy and dispersive accuracy as pertaining to Lagrangian Monte Carlo schemes implies that the optimum magnitude of Δ_E cannot, in general, be specified *a priori* (Pope 1985; Colucci *et al.* 1998). This does not diminish the capability of the scheme, but exemplifies the importance of the parameters which govern the statistics.

In an attempt to reduce the computational overhead, a procedure involving the use of non-uniform weights is also considered. This procedure allows a smaller number of particles to be imposed in regions where a low degree of variability is expected. Conversely, in regions of highly varying character, a larger number of particles is allowed. This is akin to grid compression in finite difference (or finite volume) schemes. Operationally, the particles evolve with a discrete FMDF,

$$F_N(\boldsymbol{\psi}; \boldsymbol{x}, t) = \Delta m \sum_{n=1}^{N} w^{(n)} \delta(\boldsymbol{\psi} - \boldsymbol{\phi}^{(n)}) \delta(\boldsymbol{x} - \boldsymbol{x}^{(n)}) \tag{35}$$

where $w^{(n)}$ is the weight of the nth particle and Δm is the mass of a particle with unit weight. The FMDF is the expectation of the discrete FMDF

$$F_L(\boldsymbol{\psi}; \boldsymbol{x}, t) = \Delta m \sum_{n=1}^{N} \langle w^{(n)} \delta(\boldsymbol{\psi} - \boldsymbol{\phi}^{(n)}) \delta(\boldsymbol{x} - \boldsymbol{x}^{(n)}) \rangle$$

$$= \Delta m \langle w^{(n)} \delta(\boldsymbol{\psi} - \boldsymbol{\phi}^{(n)}) \delta(\boldsymbol{x} - \boldsymbol{x}^{(n)}) \rangle \tag{36}$$

for any n ($1 \leqslant n \leqslant N$). The brackets without the subscript L represent ensemble averaging. With integration of this expression over the composition domain within an infinitesimal volume, it is possible to demonstrate that

$$\langle \rho \rangle_\ell \approx \frac{\Delta m}{\Delta V} \sum_{n \in \Delta_E} w^{(n)}, \tag{37}$$

where ΔV is the volume of the ensemble domain. The Favre-filtered value of a

transport quantity $\hat{Q}(\boldsymbol{\phi})$ is constructed from the weighted average

$$\langle Q \rangle_L \approx \frac{\sum_{n \in \Delta_E} w^{(n)} \hat{Q}(\boldsymbol{\phi}^{(n)})}{\sum_{n \in \Delta_E} w^{(n)}}. \tag{38}$$

The approximations in (37) and (38) are exact in the limit $\Delta_E \to 0$ and the number of particles within the ensemble domain becomes infinite (Pope 1985). Equation (37) implies that the filtered fluid density is directly proportional to the sum of the weights in the ensemble domain. With uniform weights, $\langle \rho \rangle_\ell \approx (\Delta m / \Delta V) N_E$ and $\langle Q \rangle_L \approx (1/N_E) \Sigma \hat{Q}(\boldsymbol{\phi}^{(k)})$ (Pope 1985) where N_E is the number of particles in the ensemble domain. Hence, with uniform weights, the particle number density decreases significantly in regions of high temperature. The implementation of variable weights allows the increase of the particle number density without a need to increase the number density outside the reaction zone.

To evaluate the chemical source terms, the fine-grained values of the temperature ($T^{(n)}$) for all particles are calculated from the composition variable $\boldsymbol{\phi}^{(n)} \equiv [Y_1^{(n)}, Y_2^{(n)}, \ldots, Y_{N_s}^{(n)}, h^{(n)}]$ and the fine-grained values of density ($\rho^{(n)}$) are determined from evaluation of the equation of state at the reference pressure p_0. The filtered pressure is obtained by the filtered equation of state. In this equation $\langle \rho \rangle_\ell$ is obtained from the finite difference solver and the correlation $\langle \mathscr{R} T \rangle_L$ is obtained by ensemble averaging in the Monte Carlo solver. In this way, the coupling between the hydrodynamic and the scalar fields is taken into account and allows the investigation of the effects of variable density. The results obtained by this scheme are identified by the label FMDF-1.

The pressure field as determined by the above procedure exhibits some spatial oscillations caused by statistical error. Since the spatial derivatives of $\langle p \rangle_\ell$ are required in the hydrodynamic solver, these oscillations can cause numerical difficulties. This is particularly exacerbated by the nature of the compressible hydrodynamic code which allows propagation of these oscillations throughout the computational domain. Our results shown below indicate that while the extent of noise in the pressure field is noticeable, it is not significant in the compositional variables. The amplitudes of the oscillations can be decreased by smoothing of the $\langle \mathscr{R} T \rangle_L$ field. An alternative procedure is also followed in which the correlation $\langle \mathscr{R} T \rangle_L$ is evaluated by the finite difference solution of its transport equation. With the assumption of constant $\mathscr{R}$, only the solution of the Favre-filtered temperature equation is required. The reaction source term in this equation is evaluated from the Monte Carlo solution. The results obtained by this scheme are identified by the label FMDF-2. While the finite difference solution of the filtered temperature is used to calculate the filtered pressure in FMDF-2, the filtered temperature can also be evaluated directly from the Monte Carlo particles. The results below indicate that the filtered temperature fields obtained by the two methods are nearly identical.

In addition, another LES is also considered in which the modelled transport equations for the filtered scalar and the generalized SGS scalar variance are simulated with the finite difference scheme. The hydrodynamic solver and the models for the SGS and mass flux are identical to those in FMDF, but the effects of SGS fluctuations in the filtered reaction rate are ignored. That is, (30) and (31) are solved via the finite difference scheme with the assumption $\langle \hat{S}_\alpha(\boldsymbol{\phi}) \rangle_L = \hat{S}_\alpha(\langle \boldsymbol{\phi} \rangle_L)$. The results based on this scheme are referred to as LES-FD. A variant of this model, in which the filtered

Method	Mean field equations	Particle properties	Particle fields used in the mean field equations	Duplicate fields
LES-FD	$\langle\rho\rangle_\ell$, $\langle u_i\rangle_L$, $\langle\boldsymbol{\phi}\rangle_L$	—	—	—
FMDF-1	$\langle\rho\rangle_\ell$, $\langle u_i\rangle_L$	$\boldsymbol{\phi}$, $\hat{\rho}(\boldsymbol{\phi})$, $\hat{\mathscr{R}}(\boldsymbol{\phi})$, $\hat{T}(\boldsymbol{\phi})$	—	$\langle\rho\rangle_\ell$
FMDF-2	$\langle\rho\rangle_\ell$, $\langle u_i\rangle_L$, $\langle\mathscr{R}T\rangle_L$	$\boldsymbol{\phi}$, $\hat{\rho}(\boldsymbol{\phi})$, $\hat{\mathscr{R}}(\boldsymbol{\phi})$, $\hat{T}(\boldsymbol{\phi})$	$\langle S_{\mathscr{R}T}\rangle_L$	$\langle\rho\rangle_\ell$, $\langle\mathscr{R}T\rangle_L$

TABLE 1. Attributes of the computational methods.

reaction rate is modelled by $\langle\hat{S}_\alpha(\boldsymbol{\phi})\rangle_L = \langle\hat{S}_\alpha(\langle\boldsymbol{\phi}\rangle_L)\rangle_L$ was also considered. However this closure did not show any improvements over LES-FD; thus it is not discussed. For non-reacting flows, the LES-FD results are used to demonstrate the consistency of the FMDF. For reacting flows, the difference between FMDF and LES-FD demonstrates the effects of the SGS fluctuations. However, this comparison does not imply that these two methods are the only means of performing LES of reacting flows; several other schemes are currently available as indicated in § 1.

It is noted that the FMDF-1 simulation procedure is similar to that typically used in PDF methods (Pope 1985; Tolpadi *et al.* 1995, 1996). The FMDF-2 procedure is proposed here for the first time. It is shown below that the pressure field as determined by this method exhibits almost no spatial oscillations, thus no smoothing is required. This scheme is starting to replace the equivalent of FMDF-1 in PDF methods (Pope 1997). The attributes of the LES-FD, FMDF-1 and FMDF-2 schemes are outlined in table 1. In this table, $S_{\mathscr{R}T}$ denotes the source term in the equation governing the transport of $\mathscr{R}T$.

5. Results

5.1. *Flows simulated*

The simulations of the following flow configurations are considered:

I. A two-dimensional temporally developing mixing layer.
II. A three-dimensional temporally developing mixing layer.
III. A two-dimensional spatially developing planar jet.
IV. A two-dimensional spatially developing mixing layer.

The objectives of the numerical simulations are to: (i) demonstrate the consistency of the Monte Carlo solution procedure, (ii) demonstrate the capabilities of the FMDF, (iii) appraise its overall performance, and (iv) highlight its deficiencies. The flow configurations I, III and IV are suitable for objectives (i) and (ii) in which two-dimensional simulations are sufficient. However, objective (iii) requires three-dimensional simulations. All flow configurations are used for objective (iv). The two-dimensional simulations are conducted to allow extensive computations for assessing the consistency and accuracy of the FMDF and the convergence of the Monte Carlo results. Both non-reacting and reacting flows are simulated, and FMDF and LES-FD are applied to the cases itemized in I–III. Some of these cases are also treated by DNS, the results of which are used to assess the performance of the FMDF. Further appraisal is made by comparison with laboratory data for the flow under item IV.

The temporal mixing layer consists of two co-flowing streams travelling in opposite directions with the same speed (Riley, Metcalfe & Orszag 1986; Jou & Riley 1989; Givi 1989). The reactants $\mathscr{A}$ and $\mathscr{B}$ are introduced into the top and the bottom streams, respectively. The length in the streamwise direction is large enough to allow for the roll-up of two large vortices and one (subsequent) pairing of these vortices. In three-dimensional simulations, the length of the domain in the spanwise direction is about 60% of that in the streamwise direction. The layer is forced via both two-dimensional and three-dimensional forcing functions (Moser & Rogers 1991; Miller, Madnia & Givi 1994; Givi 1994). The initial values of the reactants $\mathscr{A}$ and $\mathscr{B}$ at each spanwise location in three dimensional simulations are identical to those in two dimensions. In the figures presented below, x, y, z correspond to the streamwise, cross-stream and spanwise directions (in three dimensions), respectively in all the simulations.

In the planar jet, the reactant $\mathscr{A}$ is issued from a jet of width D into a co-flowing stream with a lower velocity carrying reactant $\mathscr{B}$ (Givi & Riley 1992; Steinberger, Vidoni & Givi 1993). The size of the domain in the jet flow is $0 \leqslant x \leqslant 14D$, $-3.5D \leqslant y \leqslant 3.5D$. The ratio of the co-flowing stream velocity to that of the jet at the inlet is kept fixed at 0.5. A double-hyperbolic tangent profile is utilized to assign the velocity distribution at the inlet plane. The formation of the large-scale coherent structures is expedited by imposing low-amplitude perturbations at the inlet. The frequency of these perturbations corresponds to the most unstable mode and subharmonics of this mode as determined by the linear stability analysis of spatially evolving disturbances (Michalke 1965; Colucci 1994). The characteristic boundary condition procedure developed by Poinsot & Lele (1992) is used at the inlet. This procedure facilitates evaluation of incoming waves which are necessary to satisfy the continuity equation. Zero-derivative boundary conditions are used at the free streams and the pressure boundary condition of Rudy & Strikwerda (1980) is used at the outflow.

The flow configuration in IV is the one considered in the laboratory experiments of Mungal & Dimotakis (1984). In these experiments, a heat-releasing reacting planar mixing layer composed of diatomic hydrogen in one stream and diatomic fluorine in the other stream is considered. Both reactants are diluted in nitrogen with the level of dilution determining the extent of heat release. While the laboratory flow, like all turbulent flows, is inherently three-dimensional, it is dominated by large-scale two-dimensional structures (Brown & Roshko 1974; Givi & Riley 1992; Givi 1994). We demonstrate that two-dimensional simulations are sufficient to capture the hydrodynamics features of this flow reasonably well. The computational domain considers the region 54.84 cm $\times$ 27.42 cm, which covers the whole region considered experimentally including $x = 45.7$ cm where measured data are reported. In order to mimic a 'naturally' developing shear layer, a modified variant of the forcing procedure suggested by Sandham & Reynolds (1989) is utilized. The cross-stream velocity component at the inlet is forced at the most unstable mode as well as four harmonics (both sub- and super-) of this mode. A spatial linear stability analysis was performed to determine the most unstable mode of the hyperbolic velocity profile imposed at the inlet. Sandham & Reynolds (1989) suggest the use of a random phase shift to 'jitter' the layer and to prevent periodic behaviour. A similar random phase shift procedure is imposed here; a discrete approximation of the Wiener process is applied for the phase shift at each time increment.

The flow variables are normalized with respect to selected reference quantities, denoted by the subscript r. In the temporal mixing layer, the reference quantities are the free-stream values and the reference length L_r is defined such that $\delta_{v0}/L_r = 2.83$,

where δ_{v0} is the initial vorticity thickness ($\delta_v = \Delta U/\left[\partial\overline{\langle u_1\rangle_L}/\partial y\right]_{max}$, where $\overline{\langle u_1\rangle_L}$ is the Reynolds-averaged value of the Favre-filtered streamwise velocity and ΔU is the velocity difference across the layer). In the spatially developing flows, normalization is performed with respect to the values in the high-speed stream. In the planar jet $L_r = D$. In the hydrogen–fluorine mixing layer, L_r is equal to the distance from the virtual origin to the downstream measuring station in the experiment. These quantities are used to define the Reynolds number $Re = \rho_r U_r L_r/\mu$. For the temporal mixing layer, the Reynolds number in terms of the total velocity difference across the layer ($\Delta U = 2U_r$) is $Re_{\delta_{v0}} = 5.66Re$. The non-dimensional time is given by $t^* = U_r t/L_r$.

5.2. *Reaction mechanisms*

For the flow configurations I–III, the reaction scheme is of the type $\mathscr{A} + \mathscr{B} \rightarrow \mathscr{P}$ with an Arrhenius reactant conversion, $S_{\mathscr{A}} = S_{\mathscr{B}} = -\rho k_f AB \exp(-E_a/RT)$, where k_f is the pre-exponential factor, E_a is the activation energy, and A, B denote the mass fractions of species $\mathscr{A}$, $\mathscr{B}$, respectively. The species $\mathscr{A}$, $\mathscr{B}$, $\mathscr{P}$ are assumed thermodynamically identical and the fluid is assumed to be calorically perfect. The normalized reaction rate is $S^*_{\mathscr{A}} = -\rho^* DaAB \exp(-Ze/T^*)$ in which $Ze = E_a/RT_r$ and $Da = k_f\rho_r/(U_r/L_r)$ denote the Zeldovich number and the Damköhler number, respectively. T_r denotes the reference ambient temperature. The degree of exothermicity is parameterized by the non-dimensional heat release parameter $Ce = -\Delta h^0_P/(c_p T_r)$ where Δh^0_P is the heat of reaction. Both constant-rate and temperature-dependent reactions are considered.

The reaction mechanism associated with the mixing layer experiment is more complex. The hydrogen–fluorine reaction can be represented by (Mungal & Dimotakis 1984)

$$H_2 + F_2 \rightarrow 2HF, \quad \Delta Q = 65 \text{ kcal mol}^{-1}, \tag{39}$$

where ΔQ is the heat of reaction. This reaction belongs to the more general family of hydrogen–halogen reactions (Spalding & Stephenson 1971; Chelliah 1989). The heat released in a mixture containing 1% mole fraction of F_2 and 1% mole fraction of H_2 diluted in nitrogen results in an adiabatic temperature of 93 K above the ambient (Mungal & Dimotakis 1984). The global representation in (39) is composed of a pair of second-order chain reactions and two additional reactions describing the creation and consumption of free fluorine atoms (Mungal & Dimotakis 1984)

$$H_2 + F \xrightarrow{k_1} HF + H, \quad \Delta Q = 32 \text{ kcal mol}^{-1}, \quad k_1 = 2.6 \times 10^{12} T^{0.5} \exp\left(\frac{-610}{R^0 T}\right), \tag{40}$$

$$H + F_2 \xrightarrow{k_2} HF + F, \quad \Delta Q = 98 \text{ kcal mol}^{-1}, \quad k_2 = 3 \times 10^{9} T^{1.5} \exp\left(\frac{-1680}{R^0 T}\right), \tag{41}$$

$$NO + F_2 \xrightarrow{k_3} NOF + F, \quad \Delta Q = 18 \text{ kcal mol}^{-1}, \quad k_3 = 4.2 \times 10^{11} \exp\left(\frac{-1150}{T}\right), \tag{42}$$

$$F + NO + M \xrightarrow{k_4} NOF + M, \quad \Delta Q = 57 \text{ kcal mol}^{-1}, \quad k_4 \approx 3 \times 10^{16} \text{ cm}^6 \text{ mol}^{-2} \text{ s}^{-1}, \tag{43}$$

where the reaction rate constants k_1 and k_2 are given in units of $\mathrm{cm^3\,mol^{-1}\,s^{-1}}$, T in K, and the universal gas constant R^0 in $\mathrm{cal\,mol^{-1}\,K^{-1}}$. While it is necessary to add nitric oxide to initiate reaction, the addition of excessive amounts would deplete the availability of the free F atoms. Mungal & Dimotakis (1984) indicate that keeping the product of nitric oxide and diatomic fluorine molar concentrations at 0.03% results in a rapid combustion. It was also noted that an increase of 50% in the nitric oxide concentration results in no appreciable changes in the temperature. This suggests that the hydrogen–fluorine reaction can be approximated by the limit of infinite rate chemistry. In the simulations, therefore, both finite and infinite rate models are considered. Due to the very fast rate of the reaction, the compositional change due to reaction is implemented in 10 incremental time steps for every hydrodynamic time step. These simulations with stiff reaction rates are obviously computationally intensive. The implementation of the infinite rate chemistry model (Williams 1985) is significantly less expensive. With this approximation, it may be possible to employ the assumed FDF approach (Madnia & Givi 1993). However, in order to demonstrate the validity of the FMDF, here this procedure is employed for both finite and infinite rate models.

5.3. *Numerical specifications*

The magnitude of the flow parameters considered in DNS are dictated by the resolution which can be afforded. The primary parameters are Re, Da, Ze, Ce, Sc, and Pr. In all simulations $Sc = Pr = 1$. All finite difference simulations (in both DNS and LES) are conducted on equally-spaced grid points ($\Delta x = \Delta y = \Delta z$ (for three dimensions) $= \Delta$). The highest resolution in DNS of the two-dimensional temporal mixing layer consists of 433×577 grid points which allows reliable calculations at $Re = 2000$, $Ce = 5$, $Ze = 8$, and $Da = 11.92$. The DNS of the three-dimensional temporal shear layer is conducted with a resolution of $217 \times 289 \times 133$ grid points with $Re = 400$, $Da = 1$ and $Ce = Ze = 0$. The DNS of the planar jet is performed on 1201×601 grid points and allows accurate simulations with $Re = 10\,000$, $Ce = 2.5$, $Ze = 8$ and $Da = 119.2$. The FMDF and LES-FD are conducted with lower grid resolutions. The LES of the temporal mixing layer is conducted on 37×49 and 55×73 grid points for two-dimensional simulations while resolutions of $37 \times 49 \times 23$ and $55 \times 73 \times 34$ are utilized in three-dimensional ones. The LES of the spatial jet and hydrogen–fluorine mixing layer are conducted on 201×101 grid points. A top-hat filter function (Aldama 1990) of the form

$$\left.\begin{aligned} G(\boldsymbol{x}' - \boldsymbol{x}) &= \prod_{i=1}^{N_d} \hat{G}(x_i' - x_i) \\ \hat{G}(x_i' - x_i) &= \begin{cases} 1/\Delta_G, & |x_i' - x_i| \leqslant \frac{1}{2}\Delta_G \\ 0, & |x_i' - x_i| > \frac{1}{2}\Delta_G \end{cases} \end{aligned}\right\} \tag{44}$$

is used with $\Delta_G = 2\Delta$, and N_d denotes the number of dimensions. No attempt is made to investigate the sensitivity of the results to the filter function (Vreman *et al.* 1994) or the filter size (Erlebacher *et al.* 1992).

For FMDF simulations of the temporal mixing layer, the Monte Carlo particles are initially distributed throughout the computational region. For the jet flow, the particles are supplied in the inlet region $-1.75D \leqslant y \leqslant 1.75D$. As the particles convect downstream, this zone distorts as it conforms to the flow as determined by the hydrodynamic field. In regions populated with particles, $\sum_{n \in \Delta_E} w^{(n)}$ remains proportional to the instantaneous filtered density (within statistical error). In regions

without particles, a delta-function FMDF corresponding to the free-stream composition is enforced. The simulation results are monitored to ensure the particles fully encompass and extend well beyond regions of non-zero vorticity and reaction. In the temporal mixing layer, due to flow periodicity in the streamwise and spanwise directions, if the particle leaves the domain at one of the boundaries new particles are introduced at the other boundary with the same compositional values. In the spatially evolving jet and the planar mixing layer, new particles are introduced at the inlet at a rate corresponding to the desired (imposed) local particle number density and fluid velocity. In some of the planar jet simulations and all of the hydrogen–fluorine mixing layer simulations, variable particle weights are employed. With prescription of the filtered fluid density, the particle weight is adjusted to yield the proper mass flux across the boundary. All other simulations utilize uniform weights. The sensitivity of the statistical results to the number of particles per grid cell (NPG) and the size of the ensemble domain is studied in the temporal mixing layer. The following sizes are considered: $\Delta_E = 2\Delta,\ \Delta,\ \Delta/2$.

In the FMDF simulation of the experimental mixing layer configuration, initially NPG = 5 in the free streams and gradually increases in the cross-steam direction peaking to NPG = 25 at the splitter plate ($y = 0$). This yields 20 to 100 sample points per ensemble for $\Delta_E = 2\Delta$. The particles are supplied in the region $-0.12L_r \leqslant y \leqslant 0.12L_r$ where $L_r = 45.7$ cm. The composition of incoming particles is set according to the composition of the fluid at the point of entry. The magnitudes of the Reynolds, Péclet, Damköhler and Zeldovich numbers and the velocity ratio across the layer in the simulations are the same as those in the experiment of Mungal & Dimotakis, but the maximum value of the Mach number in the simulations is 0.31 which is higher than that in the experiment. This was necessary in the compressible flow solver employed for the simulations. With the values of the physical parameters in this experiment, it is not possible to employ DNS and LES-FD for this flow, thus only FMDF results are compared with experimental data. For that FMDF-1 is used in which smoothing of $\langle \mathscr{R}T \rangle_L$ is done with a box filter consisting of 3×3 grid points with equal weights.

The simulated results are analysed both instantaneously and statistically. In the former, the instantaneous contours (snap-shots) and the scatter plots of the scalar values are considered. In the latter, the 'Reynolds-averaged' statistics are constructed from the instantaneous data. In the temporal mixing layer, the statistics are constructed from the ensemble from all the grid points in the homogeneous direction(s). In the spatially developing mixing layer and the jet flow, averaging is conducted via time sampling. All Reynolds-averaged results are denoted by an overbar. In the presentations below, the asterisk (denoting the normalized quantities) is dropped.

5.4. *Model parameters*

In the implementation of the MKEV, the magnitude of the reference velocity $\mathscr{U}_i$ is set to zero in the cross-stream and spanwise directions, and to the average of the high- and low-speed streams in the streamwise direction. Additionally, the ratio of the filter size at the secondary level to that at the grid level is $\Delta_{G'}/\Delta_G = 3$. In all simulations $C_I = 0.006$. The magnitude of C_R is 0.020 and 0.013 for two and three dimensions, respectively. The subgrid mass flux is modelled via (14). In all cases except LES of the hydrogen–fluorine mixing layer, $Pr_t = Sc_t = 0.7$. No attempt is made to determine the magnitudes of these model constants in a dynamic manner (Germano 1992). The subgrid mixing model requires the input of the constant C_Ω which also determines the SGS variances. The value $C_\Omega = 4$ is used in most simulations. In the hydrogen–fluorine configuration $Sc_t = Pr_t = 0.4$ and $C_\Omega = 6$. Some constant-density

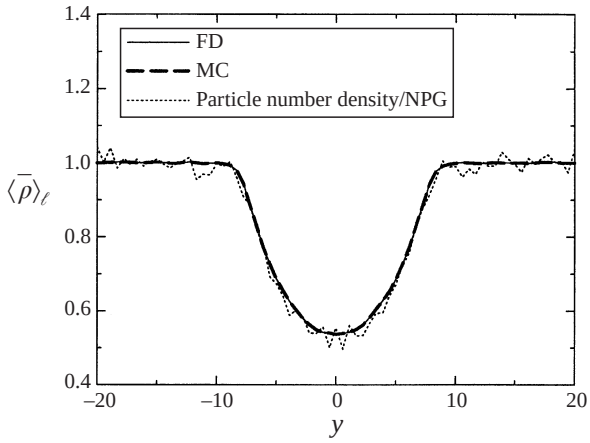

FIGURE 1. Cross-stream variation of the filtered density in the two-dimensional temporal mixing layer obtained by FMDF-1 at $t = 44$.

test simulations are also conducted in which $C_\Omega = 3$ as previously used by Colucci *et al.* (1998). The non-universality (flow dependence) of the hydrodynamic model constants (C_I, C_R, Pr_t, Sc_t) has been well recognized and was expected here. The additional constant introduced by FMDF is C_Ω, although this constant also appears if the SGS variance is considered in the conventional LES-FD. This non-universality, in general, diminishes the predictive capability of LES; however the range of the values as considered here is not very broad.

5.5. *Consistency of FMDF*

The objective in the results presented in this subsection is to demonstrate the consistency of the FMDF formulation. For this purpose, the LES results via FMDF and LES-FD are compared against each other in two-dimensional and three-dimensional temporal mixing layers. Since the accuracy of the finite difference scheme is well-established, this comparative analysis provides a means of assessing the performance of the Monte Carlo solution of the FMDF. For most of the results in this section, NPG = 50 in two dimensions and NPG = 20 in three dimensions at locations where $\langle\rho\rangle_\ell = 1$. In two dimensions, $\Delta_E = \Delta$ and in three dimensions, $\Delta_E = 2\Delta$. Several additional simulations are also performed with varying values of NPG and Δ_E to asses their effects.

Simulations of two-dimensional non-reacting temporally developing mixing layers are conducted in which the flow is initiated with non-uniform density and temperature distributions. The initial filtered density is distributed as a 'spike' at the middle of the layer. With uniform weights assigned to the Monte Carlo particles, the particle number density must remain proportional to the fluid density. This is observed in figure 1, where it is demonstrated that the filtered density evaluated from the Monte Carlo particles matches very well with that of the finite difference calculated values at the Eulerian grid points. The values generated by the finite difference solution are denoted by FD and the results generated by ensemble averaging of the Monte Carlo particles are denoted by MC. Figure 1 shows that at the final time of the simulation (when the flow has experienced the pairing of two neighbouring vortices) the Reynolds-averaged filtered density calculated by the finite difference and the Monte Carlo procedures are

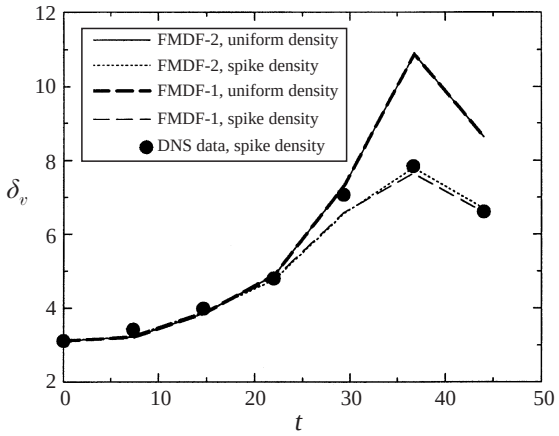

FIGURE 2. Vorticity thickness vs. time in the two-dimensional temporal mixing layer.

very close. The particle number density exhibits an appreciable degree of oscillations due to statistical errors associated with a finite sample of particles.

Figure 2 shows the temporal evolution of the vorticity thickness. When the flow starts with uniform density, the effect of thermodynamic quantities on the hydrodynamics is negligible. Thus the δ_v profiles as obtained by FMDF-1 and FMDF-2 are nearly identical. With an initial density spike, the growth of the layer is damped as expected (McMurtry, Riley & Metcalfe 1989; Jackson 1992; Colucci 1994), but the results obtained by FMDF-1 are very close to those by FMDF-2. The slight differences are due to the numerical solution procedures. The results obtained by both procedures are close to those obtained by DNS.

In figure 3, the contour plots of the resolved vorticity and temperature at the final time ($t = 44$) as obtained by FMDF-1 and FMDF-2 are shown. This figure provides a visual demonstration of the consistency of the FMDF as the results via the two FMDF procedures are similar. The difference, as expected, is exhibited by the oscillations in FMDF-1. The effect of the baroclinic torque near the braids is captured by both simulations. To exhibit the extent of the noise more clearly, the Reynolds-averaged values of the resolved pressure and the mass fraction of a conserved scalar are shown in figure 4. The most significant difference is evident in the filtered pressure field which exhibits appreciable oscillations in FMDF-1. These oscillations are reduced by application of a local least-square filter to smooth the Monte Carlo $\langle T \rangle_L$ field. This operation does not modify the other statistical quantities. Several other filter functions are also considered and their influence is summarized in figure 5 where the percentages of the differences between the values of $\langle p \rangle_\ell$ via FMDF-2 and FMDF-1 with smoothing are shown. In all cases, the difference is small (less than 2%); the most significant difference is as expected observed when no smoothing operation is applied. Figure 5 also shows that the difference is significantly decreased as the number of Monte Carlo particles is increased.

To demonstrate the consistency between the FMDF and LES-FD, a comparison is made between the moments of the mass fraction of $\mathscr{A}$ in the non-reacting temporal mixing layer with an initial density spike as obtained by the two procedures. Figure 6 shows the instantaneous contour plots of the Favre-filtered mass fraction of species $\mathscr{A}$ and figure 7 shows the Reynolds-averaged values of the moments of this mass fraction. In these simulations, the filtered temperature is calculated via FMDF-1

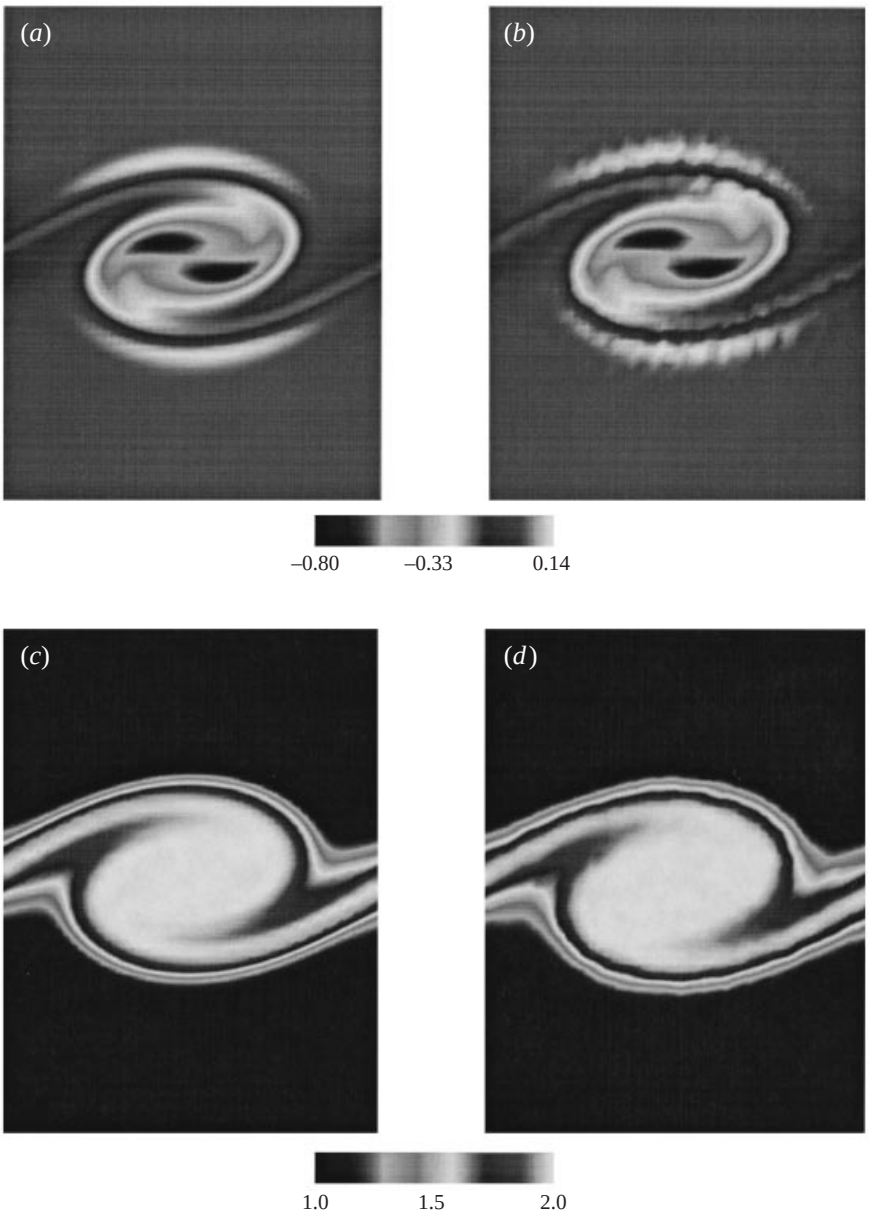

FIGURE 3. Contours of the filtered vorticity and temperature in the two-dimensional temporal mixing layer obtained by FMDF-1 (*b*, *d*) and FMDF-2 (*a*, *c*) at $t = 44$. (*a*, *b*) vorticity field, (*c*, *d*) temperature field.

without smoothing. The similarity of FMDF and LES-FD results is evident in both figures. The agreement in the first moment (figure 7*a*, *c*) is quite good even for large values of Δ_E and small values of NPG. The difference is more apparent in the subgrid variance values (figure 7*b*, *d*). However, the difference becomes smaller as Δ_E decreases.

In reactive flows, the consistency established above no longer exists since the reaction term appears in a closed form in the FMDF formulation but not in the

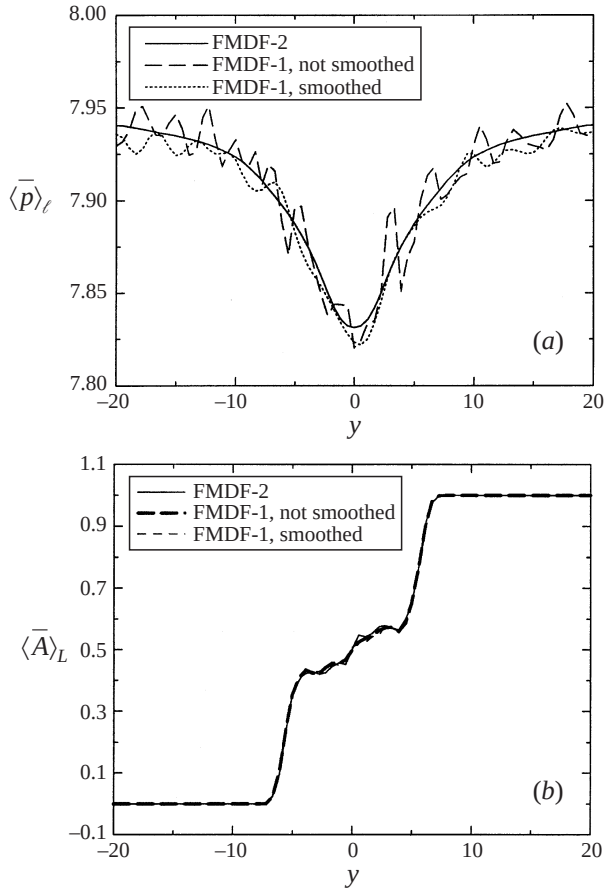

FIGURE 4. Cross-stream variation of the mean filtered quantities at $t = 44$ in the two-dimensional temporal mixing layer. (*a*) Pressure, (*b*) mass fraction of a conserved scalar.

moment equations of LES-FD. This inconsistency, which motivates the use of FMDF, is illustrated in figure 8 where the temporal evolution of the integrated 'total product' ($\delta_P(t) = \int \overline{\langle P \rangle_L}(y,t)\,\mathrm{d}y$) in a constant-density reacting temporal mixing layer with $Da = 2$ and $Ce = Ze = 0$ is shown. In these simulations, the LES resolution is 37×49 and $Re = 500$. The LES results are also compared with those obtained via DNS with 433×577 grid points. It is shown that the FMDF results are very close to those via DNS, but LES-FD significantly overpredicts the amount of products formed. Also shown in figure 8 are the results via the constant-density filtered density function (FDF) formulation (Colucci *et al.* 1998) which is suitable for this flow. The close agreement of FMDF, FDF and DNS results indicates both the consistency of the Monte Carlo solution and the relative superiority of FMDF over LES-FD.

To generalize the results above, LES of a three-dimensional temporally developing mixing layer is conducted. In this simulation, a non-reacting flow with a density spike similar to that in two dimensions is considered. The statistical results in simulations with three-dimensional forcing exhibit significant variations along the spanwise direction. The filtered pressure obtained from FMDF-1 exhibits similar trends to those obtained from FMDF-2 but does portray statistical noise. As is the case for two-dimensional simulations, the filtered mass fraction and temperature calculated by the

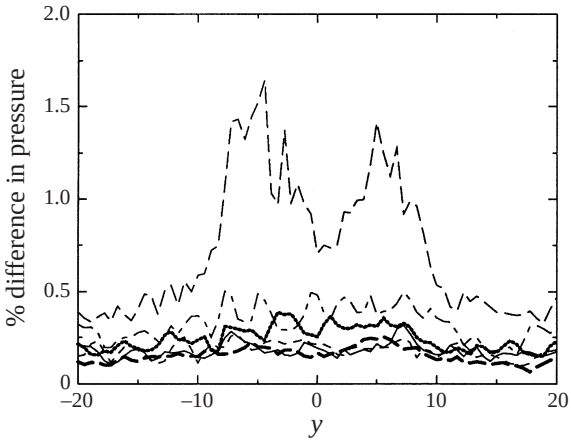

FIGURE 5. Cross-stream variation of the percentage of the difference in pressure as obtained by FMDF-2 and FMDF-1 with different smoothing in the two-dimensional temporal mixing layer at $t = 44$. Long-dashed line: no smoothing, NPG = 50 and $\Delta_E = \Delta$; dotted-dashed line: smoothed with a Gaussian filter, NPG = 50 and $\Delta_E = \Delta$; solid line: smoothed with a box filter, NPG = 50 and $\Delta_E = \Delta$; dashed line: smoothed with a local least square filter, NPG = 50 and $\Delta_E = \Delta$; Long-dashed thick line: smoothed with a Gaussian filter, NPG = 200 and $\Delta_E = \Delta$; Dotted thick line: smoothed with a Gaussian filter, NPG = 50 and $\Delta_E = 2\Delta$.

Monte Carlo solver are close to those obtained by the finite difference simulations. This is illustrated figure 9 in which scatter plots of $\langle T \rangle_L$ and $\langle A \rangle_L$ values generated by FMDF-2 are shown. The correlation coefficient between the Monte Carlo (MC) and the finite difference (FD) values is 0.999 for both sets of results shown.

5.6. *Validation via DNS data*

The objectives in this subsection are to assess the overall performance of FMDF, to appraise the validity of the submodels employed in the FMDF transport equation, and to demonstrate the capabilities of FMDF for LES of exothermic chemically reacting flows. To meet these objectives, the FMDF results are compared against DNS results of the same flow configurations with the same magnitudes of the physical parameters (*Re*, *Da*, etc.). For a meaningful comparison, the DNS data are filtered and down-sampled onto coarse grid points corresponding to those employed in FMDF. At this point it is emphasized that FMDF is not claimed to be an alternative to DNS; the comparisons made here are primarily for assessment of the FMDF. For further comparative assessments, the FMDF results are also compared with those via LES-FD. Both two-dimensional and three-dimensional simulations are considered. Unless otherwise specified, all Monte Carlo simulations presented in this section are based on the FMDF-2 formulation.

To quantify the performance of FMDF in LES of the exothermic reacting two-dimensional temporal mixing layer, in figure 10 the cross-stream variation of the Reynolds-averaged filtered temperature values are shown. In this simulation, $Da = 11.92$, $Ze = 8$ and $Ce = 5$. The FMDF results are calculated with both $\Delta_E = \Delta$ and $\Delta_E = 2\Delta$. Initially, the particle number density is set to NPG = 40 with initial uniform fluid density. The size of the ensemble domain for the evaluation of the Favre-filtered statistics does not have a significant influence on the first filtered moment. The deviation of LES-FD results from those via FMDF and/or DNS is evident. This behaviour is observed at all times for all the cases considered. It is expected that the

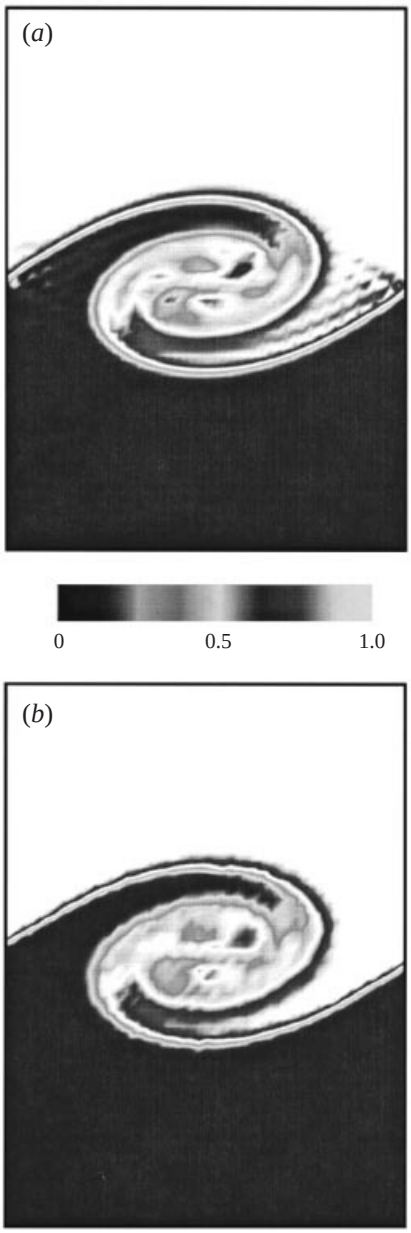

FIGURE 6. Contours of the filtered values of the conserved scalar at $t = 44$ in the two-dimensional temporal mixing layer as obtained by (*a*) LES-FD, (*b*) FMDF.

difference between DNS and LES-FD results would be even more as the magnitude of the Damköhler number and/or Reynolds number increases (Colucci *et al.* 1998). Figure 10 shows that for this flow with a rather significant variation of temperature, the averaged filtered temperature is predicted well by FMDF. Comparatively, LES-FD overpredicts the filtered temperature values. While the finite difference solution of the filtered temperature is used to calculate the filtered pressure in the FMDF-2, the filtered temperature can also be evaluated directly from the ensemble of the Monte

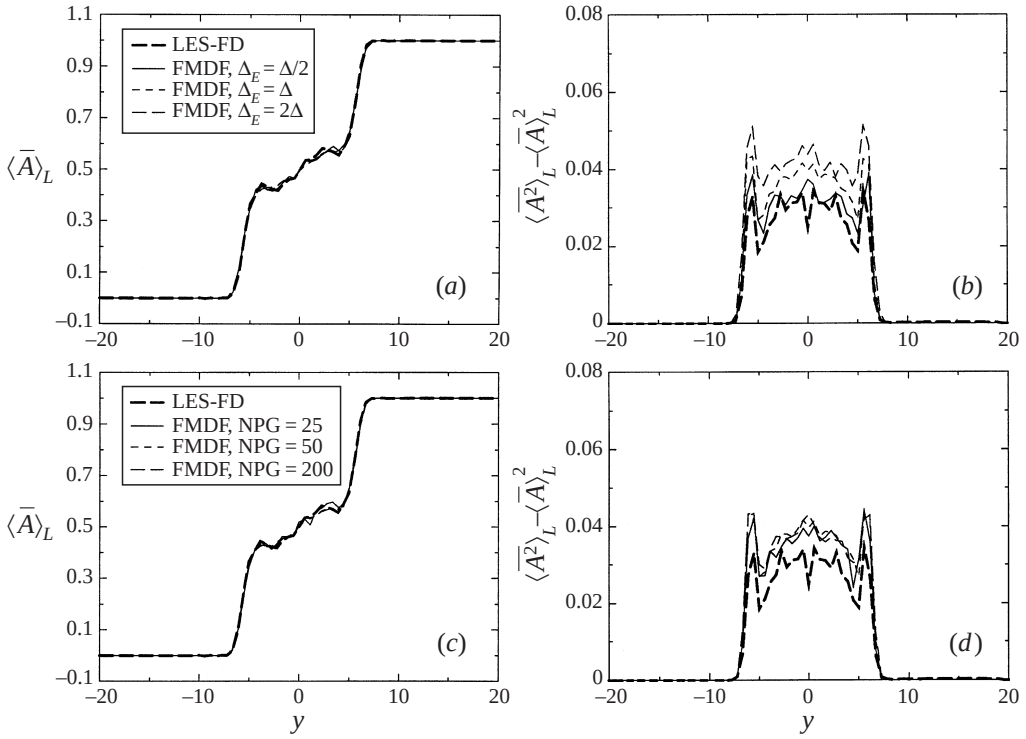

FIGURE 7. Cross-stream variation of the mean filtered scalar (a, c) and the generalized variance of the conserved scalar (b, d) in the two-dimensional temporal mixing layer.

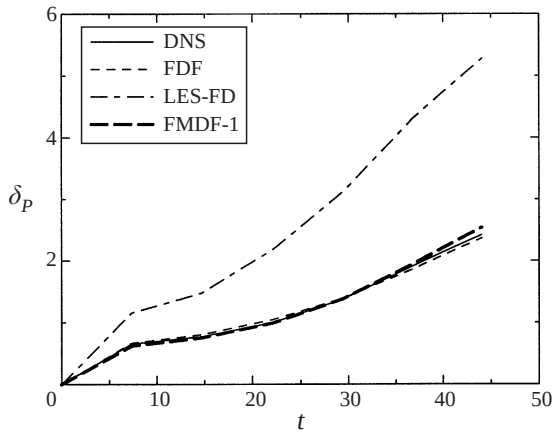

FIGURE 8. Total product variation with time in the two-dimensional temporal mixing layer.

Carlo elements. Figure 10 indicates that the evaluation of the filtered temperature in this way (denoted by MC ensemble) is consistent with that obtained by FMDF-2.

The results of the spatially developing jet flow are shown in figures 11–17 in which several issues pertaining to the Monte Carlo simulation are addressed. Figures 11 and 12 show the instantaneous contours of the filtered pressure and the filtered temperature values, respectively. Parts (*a*), (*b*), and (*c*) of these figures correspond to results with FMDF-1 without smoothing of the temperature field, FMDF-1 with smoothing, and

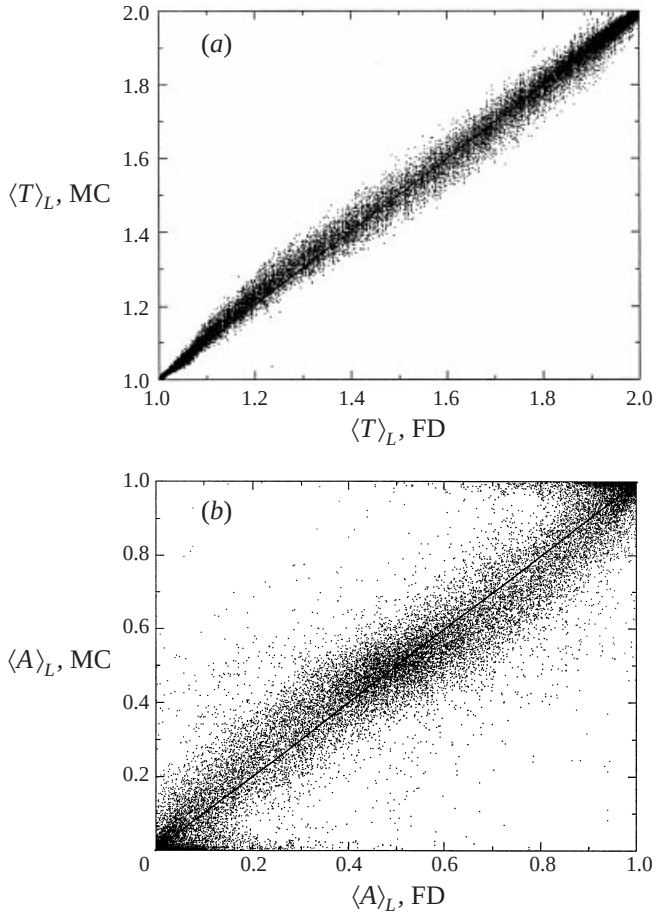

FIGURE 9. Scatter plots of the filtered quantities as obtained by the Monte Carlo (MC) solution vs. those via the finite difference (FD) solution in the three-dimensional temporal mixing layer: (*a*) temperature, (*b*) the conserved mass fraction.

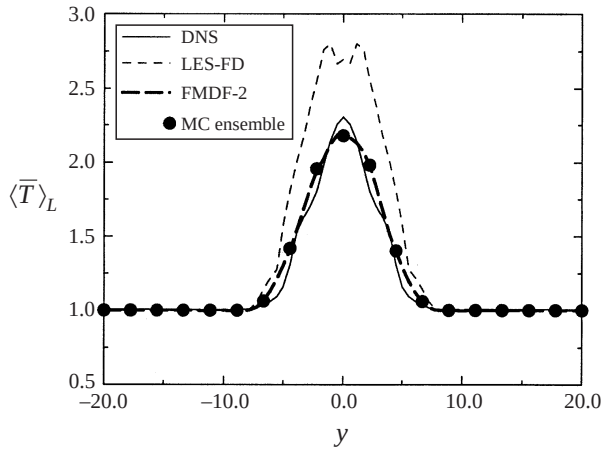

FIGURE 10. Cross-stream variation of the normalized filtered temperature in the two-dimensional temporal mixing layer.

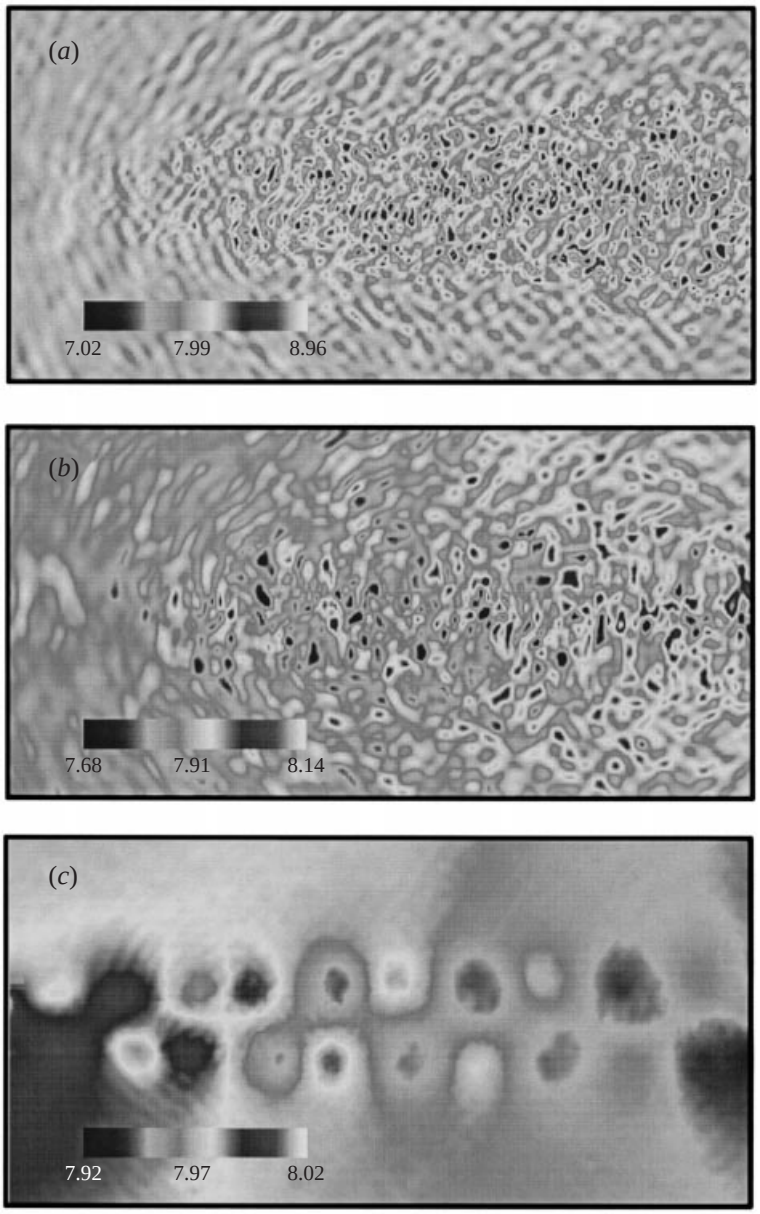

FIGURE 11. Contours of the normalized filtered pressure in the planar jet: (*a*) FMDF-1 with no smoothing of the filtered temperature, (*b*) FMDF-1 with smoothed filtered temperature with a box filter, (*c*) FMDF-2.

FMDF-2, respectively. While the temperature fields as obtained by all three procedures are similar, the differences between the pressure fields are noticeable. The behaviour portrayed in figure 11(*c*) is physical, whereas the oscillations observed in figure 11(*a*, *b*) could cause numerical problems. While these oscillations did not cause problems here, figure 11 shows that FMDF-2 is more robust and is recommended for both LES and PDF simulations. Figure 13 shows that the instantaneous particle number density and the filtered fluid density calculated by FMDF are highly correlated in these

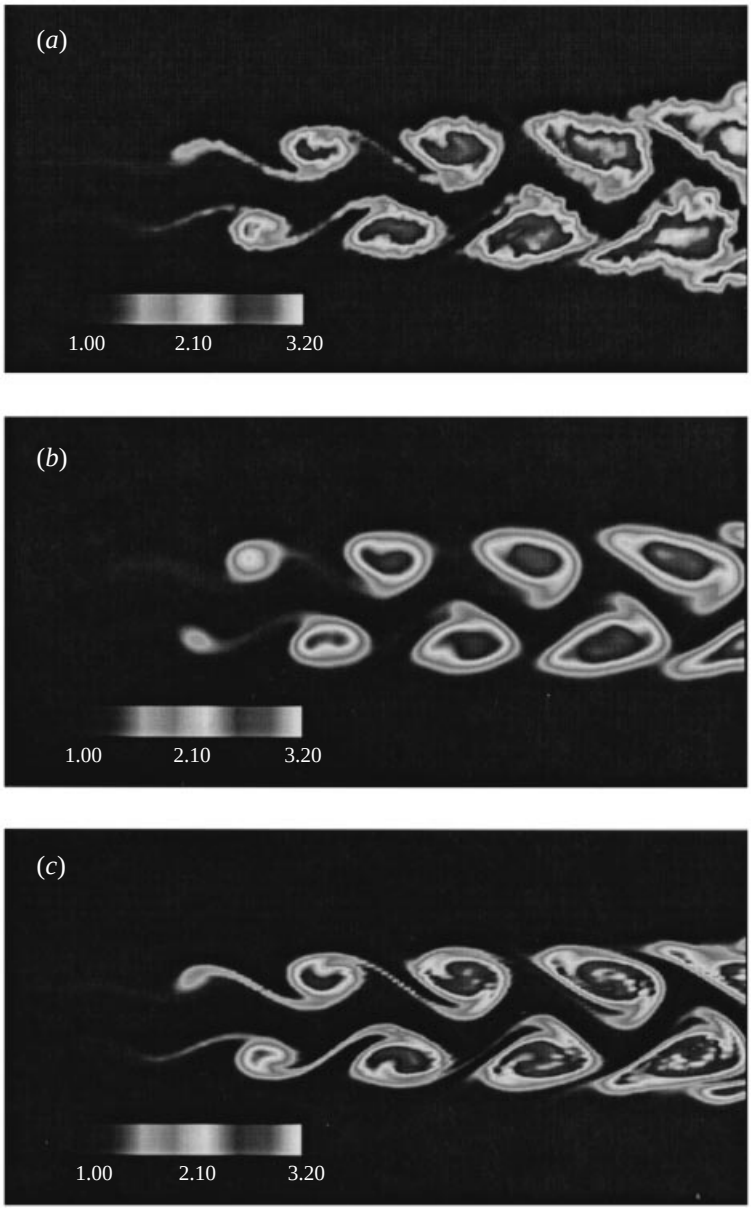

FIGURE 12. Contours of the normalized filtered temperature in the reactive planar jet: (*a*) FMDF-1 with no smoothing of the filtered temperature, (*b*) FMDF-1 with smoothed filtered temperature with a box filter, (*c*) FMDF-2.

simulations in which uniform particle weights are employed. It is noted that the particle number density is lowest in the high-temperature reaction zones. Figure 14 shows the results via variable weights. It is observed in figure 14(*a*) that there is a higher concentration of particles in the reaction zones in comparison to the case with uniform weights. The particle mass density shown in figure 14(*b*) is highly correlated with the filtered fluid density (figure 14*c*). A comparison between figures 13(*b*) and 14(*c*) indicates that despite the significant difference in the total number of particles

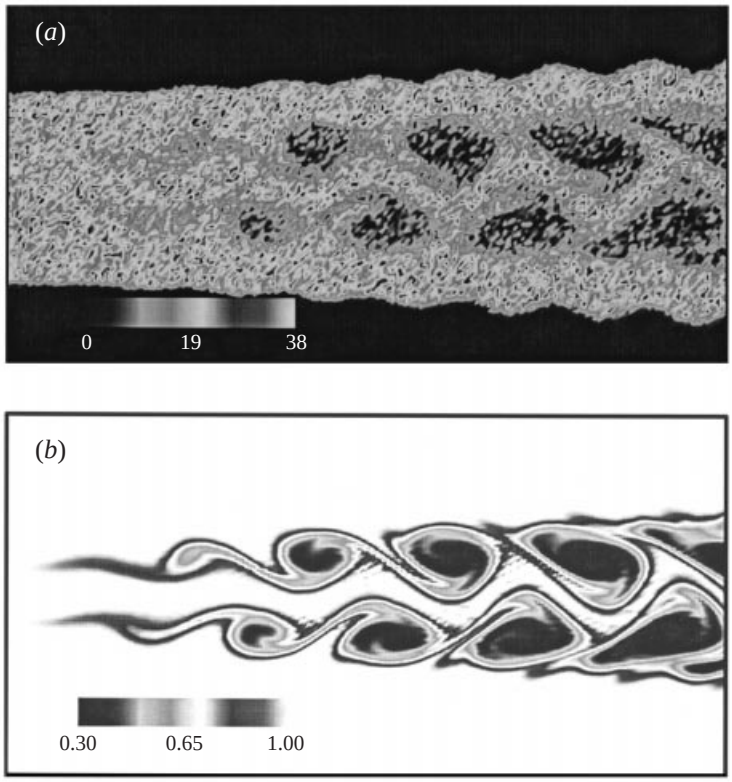

FIGURE 13. Contours of (*a*) the particle number density, (*b*) the fluid filtered density in the reactive planar jet simulations with uniform weights.

and particle weighing procedures, the filtered density fields are nearly identical in the two simulations. This similarity is also reflected in the streamwise variations of the total product ($\delta_P(x) = \int \overline{\langle P \rangle_L}(x, y)\,\mathrm{d}y$) in figure 15. The results via both procedures are nearly identical and are superior to LES-FD in matching with DNS results. The computational time in the simulations with variable weights is about half of that in simulations with equal particle weights.

As indicated previously, the essential difference between FMDF and LES-FD is due to the ability of FMDF in accounting for the SGS scalar fluctuations. To demonstrate this explicitly, in figure 16, the contour plots of the 'SGS unmixedness' defined as $\langle \rho \rangle_\ell \left[\langle \hat{S}(\boldsymbol{\phi}) \rangle_L - \hat{S}(\langle \boldsymbol{\phi} \rangle_L) \right]$ are shown. It is observed that the FMDF results are in good agreement with DNS. The contribution of the SGS unmixedness to the total filtered reaction rate is expected to increase as the magnitudes of *Re*, *Da*, *Ce* increase. Therefore, it is anticipated that the difference between DNS and LES-FD results would be even more with increased values of these parameters. Scatter data of the instantaneous product mass fraction P vs. the mixture fraction Z are presented in figure 17. These data are gathered at the final time of the simulations including the results within the region $x \geqslant 3.5D$. Both the DNS (figure 17*a*) and FMDF-2 (figure 17*b*) exhibit significant scatter indicative of appreciable finite rate chemistry effects. The FMDF is able to capture the scatter reasonably well. It is important to note that while the fine-grained values associated with the particles may be interpreted as instantaneous realizations, conventional LES cannot offer such 'de-filtered' information.

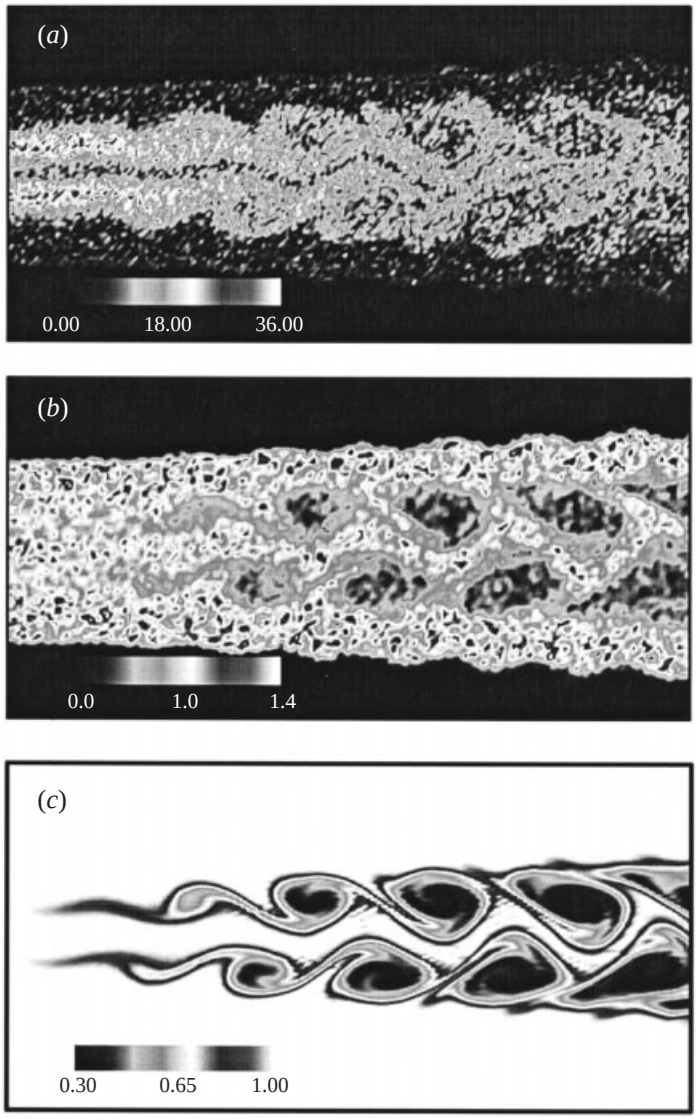

FIGURE 14. Contours of (*a*) the particle number density, (*b*) the particle mass density, (*c*) the fluid filtered density in the reactive planar jet simulations with variable weights.

The major conclusions drawn from the two-dimensional results are confirmed in three-dimensional simulations. In figure 18, the time variation of the total product as predicted by FMDF of the constant-density temporally developing reacting mixing layer is compared with DNS and LES-FD results. Consistent with the two-dimensional results, the total product predicted by FMDF is closer to DNS in comparison to that of LES-FD. With increased resolution in LES, the difference between DNS and LES-FD is less, but the FMDF results are not significantly modified.

5.7. *Validation via laboratory data*

The experiments of Mungal & Dimotakis (1984) were conducted with several values of the equivalence ratio, $\phi = c_{02}/c_{01}$ where c_0 refers to the free-stream molar concen-

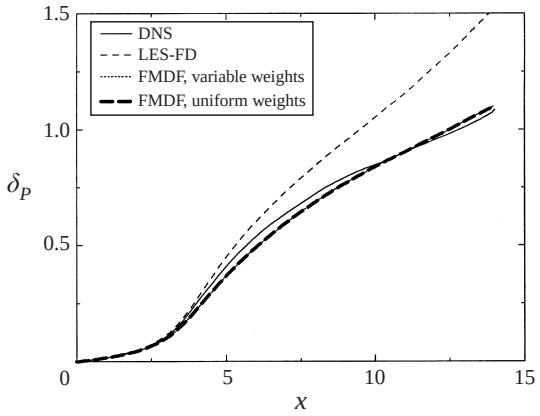

FIGURE 15. Streamwise variation of the total product in the reactive planar jet.

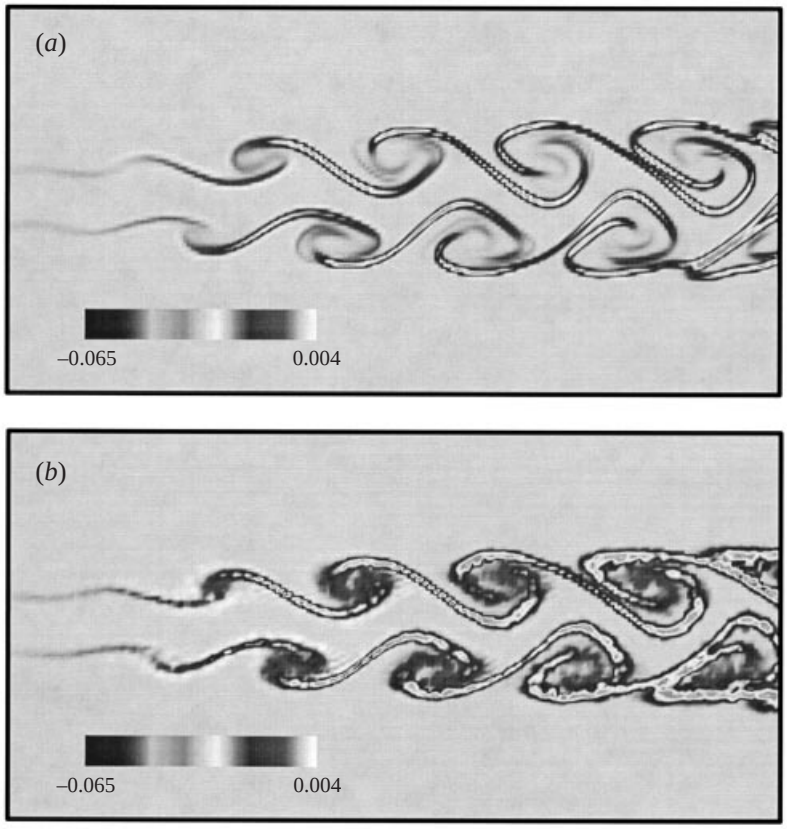

FIGURE 16. Contours of the normalized instantaneous SGS unmixedness in the reactive planar jet: (*a*) DNS, (*b*) FMDF.

tration and the subscripts 1 and 2 denote the reactants in the high- and the low-speed streams, respectively. Equivalence ratios of 1, 2, 4 and 8 were considered. In addition, 'flip' experiments were also conducted in which inverse values of the equivalence ratio ($\phi = 1, \frac{1}{2}, \frac{1}{4}$ and $\frac{1}{8}$) were considered. All of these cases are considered in the

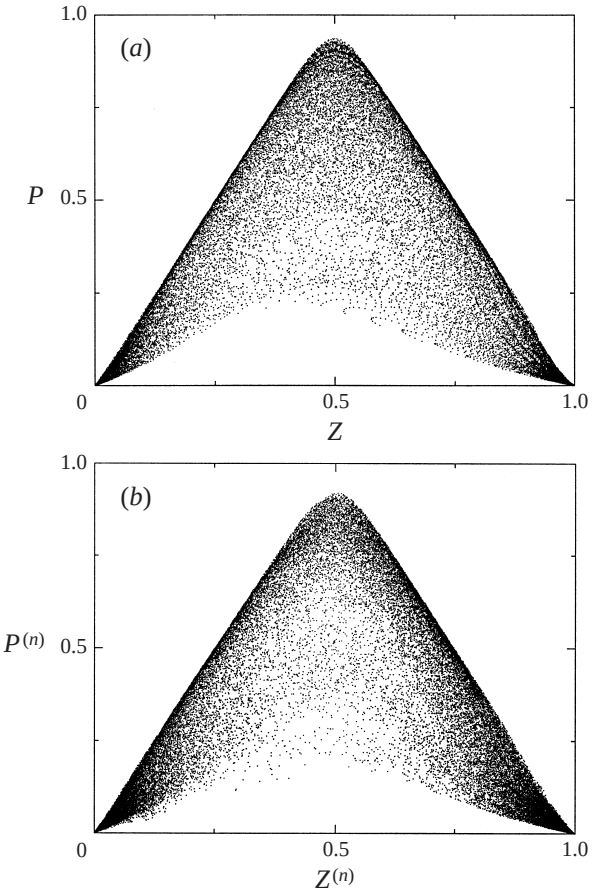

FIGURE 17. Scatter plot of the product mass fraction vs. the mixture fraction in the reactive planar jet: (*a*) DNS, (*b*) FMDF.

simulations by FMDF-1. The implementations of DNS and LES-FD are not possible for this flow.

Figure 19 displays the contour plots of the instantaneous and the Reynolds-averaged values of the filtered temperature field for the case with $\phi = 1$. In this simulation, the finite rate reaction scheme is employed. The peak value of the instantaneous temperature field approaches, but is lower than, the adiabatic flame temperature. This is due to the filtering of the temperature field. The peak values of the time-averaged temperature values are considerably lower than that of the adiabatic flame temperature, an intuitive fact indicated by Mungal & Dimotakis (1984) and also by Wallace (1981). However, a large number of individual particles do indeed approach the adiabatic limit.

The FMDF predictions are compared with experimental results both qualitatively and quantitatively. Figure 20 shows the time history of the temperature at several cross-stream locations as obtained by FMDF. Each vertical increment represents temperature values ranging from the ambient to the maximum attained instantaneous temperature (T_{max}). These time traces are qualitatively similar to those measured experimentally (Mungal & Dimotakis 1984). One notable difference is observed near the middle region of the layer. In this region, there are instances when the simulations

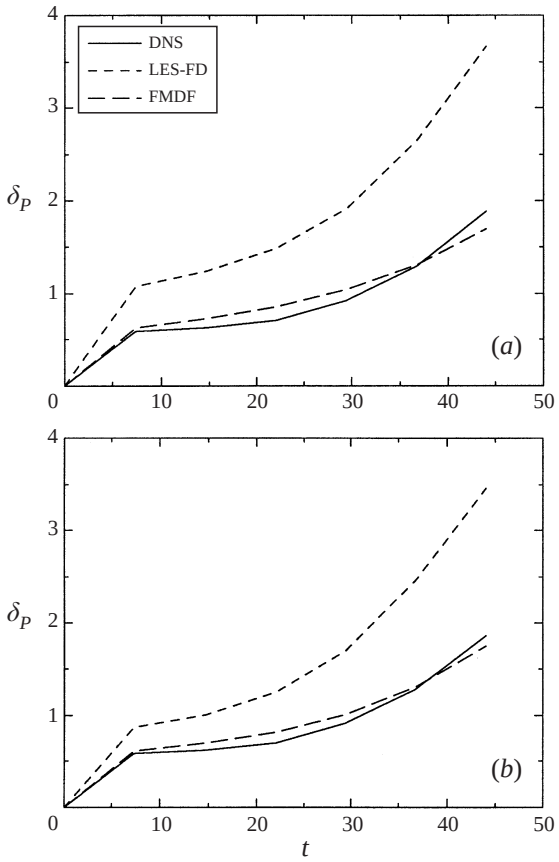

FIGURE 18. Total product vs. time in the three-dimensional temporal mixing layer: (*a*) lower LES resolution ($37 \times 49 \times 23$), (*b*) higher LES resolution ($55 \times 73 \times 34$).

exhibit near-ambient temperature values (cold fluid). While there is some evidence of this behaviour in the experiments, it is more pronounced in the simulations. This is partly attributed to the two-dimensional nature of the simulations as the small-scale mixing present in three dimensions tends to provide a more effective mixing (Miller *et al.* 1994). For this reason it is expected that the minimum values of the time-averaged temperature in the vicinity of $y = 0$ will be slightly lower than those measured experimentally. Another reason for this difference is that the cold wire probes may include some thermal lag and conduction errors (Scadron & Warshawsky 1952; Paranthoen, Petit & Lecordier 1982; Mungal & Dimotakis 1984) manifesting in an artificial 'smoothing' effect in the measured temperature values.

For a quantitative comparison, in figure 21 the cross-stream variations of the Reynolds-averaged temperature rise normalized by the adiabatic temperature rise (T_a) are shown. The quantity δ_1 denotes the distance between the points where the cross-stream mean temperature rise is 1% of the maximum mean temperature rise and y_0 is the cross-stream location where the time-averaged streamwise velocity is the average of the high- and low-speed velocities. No attempt is made to de-filter the LES results and $\langle T \rangle_L$ is directly compared to experimental data. The agreement between the FMDF and experimental data is good. Also shown in this figure are the results based on the FMDF with the infinite reaction rate model. As expected, the

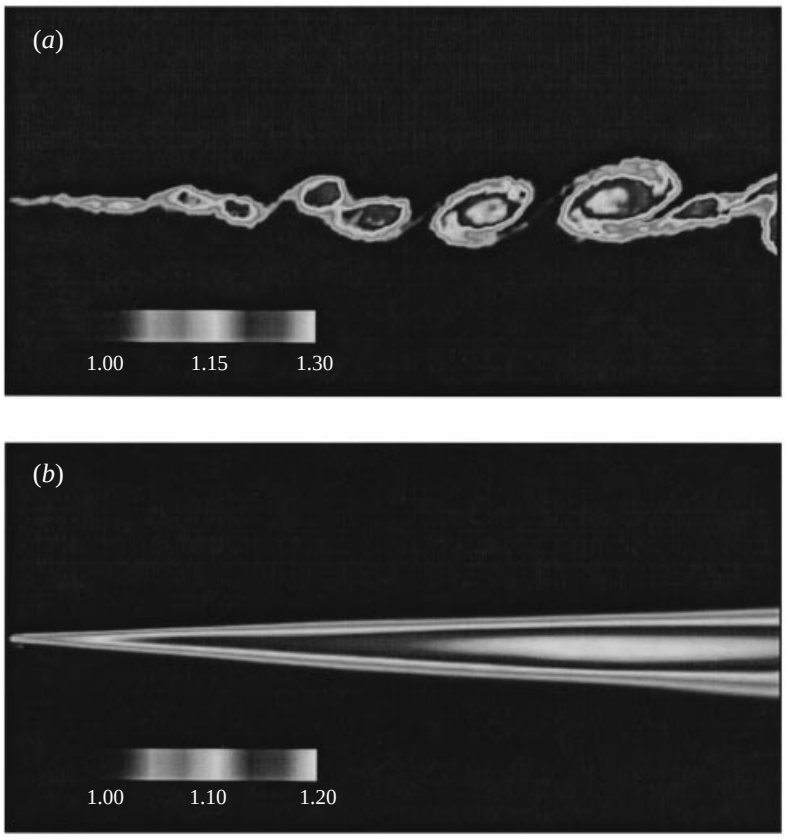

FIGURE 19. Contour plots of (*a*) instantaneous Favre-filtered temperature, (*b*) time-averaged Favre-filtered temperature for $\phi = 1$ in the hydrogen–fluorine mixing layer. The values are normalized by T_r.

results are very close to those of the finite rate simulation, but the computational cost is significantly less. In this particular case, the time requirement for FMDF simulations with the infinite rate chemistry is approximately 16% of that for the finite rate chemistry simulations. Due to this lower cost, and the confidence in the infinite rate model, the remaining simulations are conducted with this model.

To demonstrate the flip effect, figure 22 shows the cross-stream variation of the normalized temperature for all equivalence ratios (the simulations with $\phi = 1$ are repeated). Two observations are made consistent with the experimental results: (i) the peak value of the mean temperature in each of the experiments is different from that in the corresponding flip experiment, although the adiabatic flame temperature is the same; (ii) the peak temperature value shifts toward the lean reactant stream. Since the only difference between each of the two cases is the interchange of the low- and high-speed reactants, the reason for this behaviour is the different entrainment processes (Mungal & Dimotakis 1984). Additionally, with the exception of the two cases with $\phi = 1$, the peak temperature is higher for equivalence ratios greater than one compared to the reciprocal equivalence ratios. Consistent with the experimental results, the peak normalized temperature reaches a maximum for an equivalence ratio in the range $1 \leqslant \phi \leqslant 2$. These trends are more clearly portrayed in figure 23(*a*), which Mungal & Dimotakis (1984) refer to as 'inferred' temperature profiles. These reflect

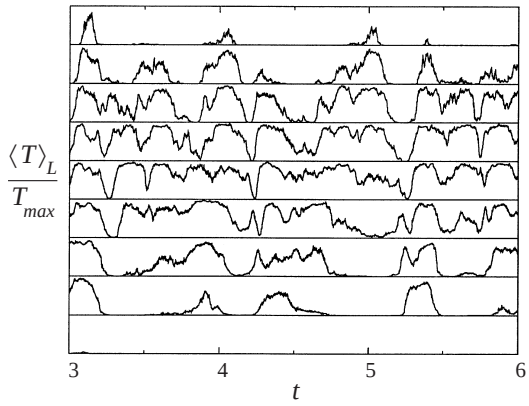

FIGURE 20. Time history of the instantaneous Favre-filtered temperature in the hydrogen–fluorine mixing layer at several cross-stream locations.

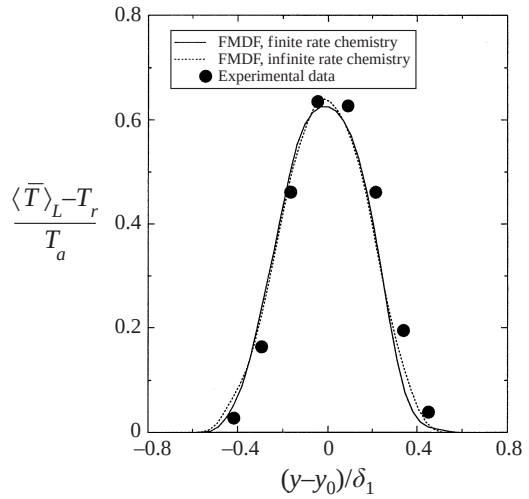

FIGURE 21. Cross-stream variation of the normalized mean temperature for $\phi = 1$ in the hydrogen–fluorine mixing layer.

the temperature if the high-speed reactant was fixed at 1% molar concentration while the low-speed stream was varied from $\frac{1}{8}$% to 8% to obtain the desired equivalence ratios. This figure supports the conclusion of Mungal & Dimotakis (1984) that there exists an asymptotic limit to the amount of products formed as the high-speed reactant is burned to completion. A similar behaviour is exhibited in figure 23(*b*) in which the inferred temperature profiles are shown for the situation in which the low-speed reactant is fixed at 1% and the high-speed reactant is varied to obtain the same equivalence ratios.

Further quantitative comparison between the FMDF and experimental results is made in figure 24 which shows the variation of the normalized product thickness with the equivalence ratio. The product thicknesses are defined as (Mungal & Dimotakis 1984)

$$\delta_{p1} = \int_{-\infty}^{+\infty} \frac{C_p\overline{\langle T(y)\rangle_L}}{c_{01}\Delta Q}\,\mathrm{d}y, \quad \delta_{p2} = \int_{-\infty}^{+\infty} \frac{C_p\overline{\langle T(y)\rangle_L}}{c_{02}\Delta Q}\,\mathrm{d}y, \tag{45}$$

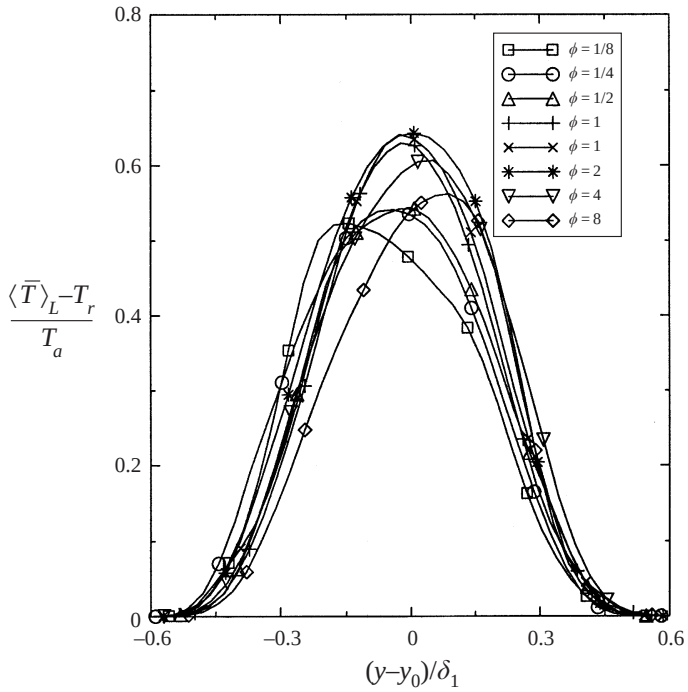

FIGURE 22. Cross-stream variation of the normalized mean temperature for all equivalence ratios in the hydrogen–fluorine mixing layer.

where C_p is the molar heat capacity of the carrier gas. Figure 24(a) indicates that the FMDF predicts the extent of product formation reasonably well over a wide range of equivalence ratios. At low values of ϕ, the amount of products varies nearly linearly as the low-speed reactant is consumed when excessive amounts of the high-speed reactant are present. At high values of the equivalence ratio, the product thickness approaches an asymptotic value as the reaction progress is inhibited by a lack of high-speed reactant relative to the amount of reactant in the low-speed stream. Figure 24(b) demonstrates a similar agreement between the experimental and the FMDF results.

5.8. *Computational requirements*

To appraise the computational requirements of the FMDF, the computational times for some of the cases are monitored. Table 2 lists the normalized CPU times required for the simulations of the reacting two-dimensional planar jet and the reacting three-dimensional temporally developing mixing layer. These cases are selected since simulations via all three schemes (FMDF, LES-FD and DNS) are conducted. The computational times listed for FMDF are those associated with FMDF-2, although the increase in cost over FMDF-1 is not very significant. Obviously the overhead of the FMDF simulation is extensive compared to LES-FD; nevertheless, the computational time for FMDF simulation is significantly less than that of DNS. Again it is emphasized that FMDF is not claimed to be an alternative to DNS; neither it is claimed that the FMDF is capable of reproducing all DNS results. However, the close proximity of values obtained via FMDF and DNS, and the substantially lower computational costs of FMDF makes it a viable tool for simulations of reacting flow systems for which DNS is not possible.

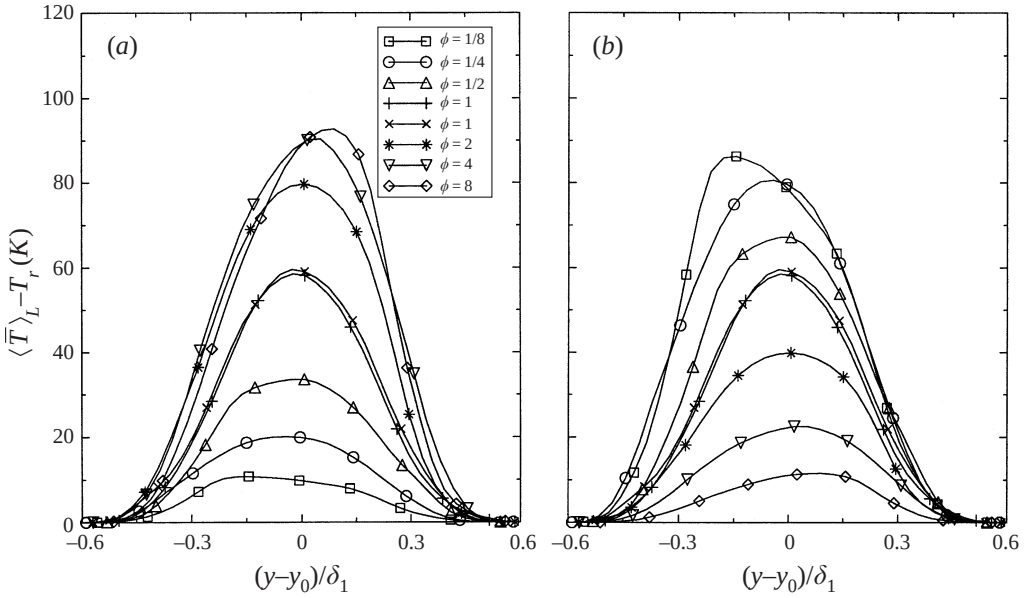

FIGURE 23. Cross-stream variation of the 'inferred' mean temperature profiles for (*a*) 1% high-speed mole fraction, (*b*) 1% low-speed mole fraction for all equivalence ratios in the hydrogen–fluorine mixing layer.

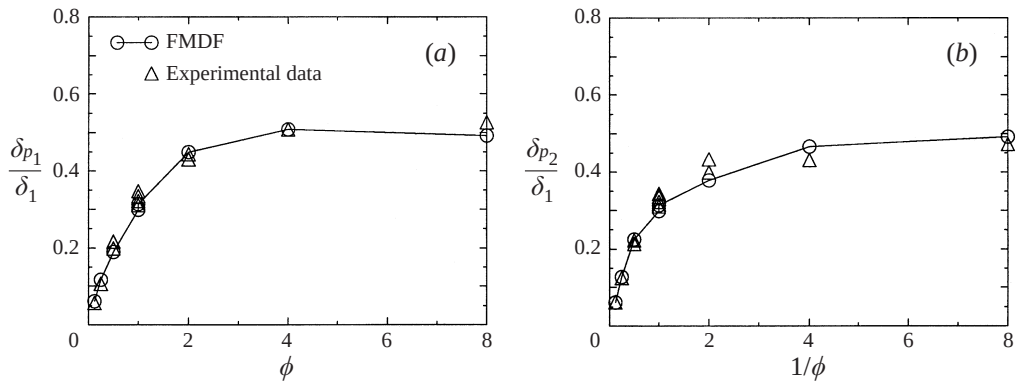

FIGURE 24. Normalized product thickness variation with equivalence ratio in the hydrogen–fluorine mixing layer: (*a*) δ_{p1} vs. the equivalence ratio, (*b*) δ_{p2} vs. the inverse equivalence ratio.

6. Summary and concluding remarks

The basic objective of this work is to develop a methodology for large-eddy simulation (LES) of turbulent reacting flows, with the inclusion of exothermicity and variable-density effects. The methodology is termed the 'filtered mass density function' (FMDF) and is based on the extension of the 'filtered density function' (FDF) developed previously for LES of constant-density, reacting, isothermal flows (Colucci *et al.* 1998). The procedure for this extension is similar to that used in probability density function (PDF) methods in Reynolds-averaging procedures (Pope 1985). Here the FMDF is considered for treatment of scalar variables. A transport equation is developed for the FMDF in which the unclosed terms, similar to PDF methods, are due to SGS convection and mixing. The former is modelled via the

	2D		3D	
Simulation	Grid resolution	Normalized CPU time†	Grid resolution	Normalized CUP time‡
DNS	1201×601	242.5	$217 \times 289 \times 133$	182.71
FMDF	201×101	7.62	$55 \times 73 \times 34$	7.64
LES-FD	201×101	1	$55 \times 73 \times 34$	1

TABLE 2. The computational times for two-dimensional planar jet simulations and three-dimensional temporal mixing layer simulations.

† Unit corresponds to 760 seconds on a Cray-C90.
‡ Unit corresponds to 655 seconds on a Cray-C90.

gradient diffusion model as done in most LES of non-reacting flows (Galperin & Orszag 1993); the latter is closed via the IEM model as typically used in PDF methods (Pope 1985).

The modelled FMDF transport equation is solved numerically via a Lagrangian Monte Carlo scheme in which the solutions of the equivalent stochastic differential equations (SDEs) are obtained. Two Monte Carlo procedures are considered. The first (FMDF-1) is similar to that typically used in PDF methods (Pope 1985; Tolpadi *et al.* 1995, 1996). The second (FMDF-2) is new. Both schemes preserve the Itô–Gikhman nature of the SDEs and provide a reliable solution for the FMDF. The second scheme is more robust in dealing with the statistical noise generated by the Monte Carlo scheme. The consistency of the FMDF, the convergence of its Monte Carlo solutions, the advantages and drawbacks of the FMDF as well as the performance of the closures employed in the FMDF transport equation are assessed. This is done via extensive comparisons between the results obtained by the Monte Carlo procedure and the finite difference solution of the transport equations of the first two filtered moments of scalar quantities (LES-FD). In non-reacting flows, the consistency and convergence of the Monte Carlo solution is demonstrated by good agreements of the first two SGS scalar moments with those obtained by LES-FD. The performance of FMDF and its superiority over LES-FD are demonstrated by comparison with direct numerical simulation (DNS) results of two-dimensional and three-dimensional temporally developing mixing layers, and a two-dimensional spatially developing jet. In all cases the FMDF results are shown to be in closer agreement with the DNS data than are the LES-FD results in which the influence of the SGS fluctuations on the reaction rate is ignored.

The performance of the FMDF is further appraised by comparison against the experimental data of Mungal & Dimotakis (1984) of a spatially developing mixing layer involving the exothermic hydrogen–fluorine reaction. The FMDF is considered via both finite rate and infinitely fast chemistry. The treatment of the former with a stiff reaction source term is computationally expensive, but comparison of the results with those of the latter gives confidence in the less costly infinite rate procedure. The results produced by both methods compare favourably with experimental data and some qualitative features, such as the 'flip effect', are captured by the FMDF simulation.

In addition to the those in the hydrodynamic closure, there are three constants for the LES of scalar quantities: Sc_t and Pr_t for the SGS convective fluxes of the mass fraction and the temperature, respectively, and C_Ω as appears in the SGS mixing

model. Based on the present results and those of Colucci *et al.* (1998) for a variety of different flows (two-dimensional and three-dimensional, constant and variable density, different chemistry schemes, etc.) it seems that $Sc_t = Pr_t \approx 0.4$–0.7, $C_\Omega \approx 3$–6. The predictive capability of the FMDF can be improved by future developments in PDF methods.

While the FMDF method is computationally more expensive than conventional LES method, it is much more advantageous for treating reacting flows. The computational overhead is tolerable for simulations of complex reacting flows for which DNS is not feasible.

This work is part of a research program sponsored by the NASA Langley Research Center under Grant NAG-1-1122 to SUNY-Buffalo and Grant NAG-1-1542 to Cornell University. Dr J. Philip Drummond is the Technical Monitor of this program. Acknowledgment is also made to the Donors of the Petroleum Research Funds administrated by the American Chemical Society for their support under Grant ACS-PRF 32892-AC9 to SUNY-Buffalo. Additional support for the work at Cornell is provided by the AFOSR under Grant F49620-97-1-0126. Computational resources are provided by the NCSA at the University of Illinois and by the CCR at SUNY-Buffalo.

REFERENCES

Aldama, A. A. 1990 *Filtering Techniques for Turbulent Flow Simulations.* Lecture Notes in Engineering, vol. 49. Springer.

Bardina, J., Ferziger, J. H. & Reynolds, W. C. 1983 Improved turbulence models based on large eddy simulations of homogeneous, incompressible, turbulent flows. *Dept of Mech. Engng Rep.* TF-19. Stanford University, Stanford, CA.

Bilger, R. W. 1982 Molecular transport effects in turbulent diffusion flames at moderate Reynolds number. *AIAA J.* **20**, 962–970.

Borghi, R. 1988 Turbulent combustion modeling. *Prog. Energy Combust. Sci.* **14**, 245–292.

Branley, N. & Jones, W. P. 1997 Large eddy simulation of a turbulent non-premixed flame. In *Proc. Eleventh Symp. on Turbulent Shear Flows*, pp. 21.1–21.6. Grenoble, France.

Brown, G. L. & Roshko, A. 1974 On density effects and large structure in turbulent mixing layers. *J. Fluid Mech.* **64**, 775–816.

Carpenter, M. H. 1990 A high-order compact numerical algorithm for supersonic flows. In *Twelfth Intl Conf. on Numerical Methods in Fluid Dynamics* (ed. K. W. Morton). Lecture Notes in Physics, vol. 371, pp. 254–258. Springer.

Chelliah, H. K. 1989 Asymptotic analysis of the structures and characteristics of flames. PhD thesis, Princeton University.

Colucci, P. J., Jaberi, F. A., Givi, P. & Pope, S. B. 1998 Filtered density function for large eddy simulation of turbulent reacting flows. *Phys. Fluids* **10**, 499–515.

Colucci, P. J. 1994 Linear stability analysis of density stratified parallel shear flows. *AIAA Paper* 94-0011.

Cook, A. W. & Riley, J. J. 1994 A subgrid model for equilibrium chemistry in turbulent flows. *Phys. Fluids* **6**, 2868–2870.

Cook, A. W., Riley, J. J. & deBruynKops, S. M. 1997*a* A sub-grid model for nonpremixed turbulent combustion. In *Proc. Eleventh Symp. on Turbulent Shear Flows*, pp. 16.13–16.18. Grenoble, France.

Cool, T. A., Stephens, R. R. & Shirley, J. A. 1970 HCl, HF, and DF partially inverted CW chemical lasers. *J. Appl. Phys.* **41**, 4038–4050.

DesJardin, P. E. & Frankel, S. H. 1998 Large eddy simulation of a turbulent nonpremixed reacting jet: Application and assessment of subgrid-scale combustion models. *Phys. Fluids* **10**, 2298–2314.

Dopazo, C. & O'Brien, E. E. 1976 Statistical treatment of non-isothermal chemical reactions in turbulence. *Combust. Sci. Tech.* **13**, 99–112.

Drummond, J. P. 1991 Supersonic reacting internal flow fields. In *Numerical Approaches to Combustion Modeling* (ed. E. S. Oran & J. P. Boris). Progress in Astronautics and Aeronautics, chap. 12, pp. 365–420. AIAA.

Eidson, T. M. 1985 Numerical simulation of the turbulent Rayleigh–Benard problem using subgrid modelling. *J. Fluid Mech.* **158**, 245–268.

Erlebacher, G., Hussaini, M. Y., Speziale, C. G. & Zang, T. A. 1992 Toward the large eddy simulation of compressible turbulent flows. *J. Fluid Mech.* **238**, 155–185.

Fox, R. O. 1996 Computational methods for turbulent reacting flows in chemical process industry. *Revue De L'Institut Francais Du Petrole* **51**, 215–246.

Frankel, S. H., Adumitroaie, V., Madnia, C. K. & Givi, P. 1993 Large eddy simulations of turbulent reacting flows by assumed PDF methods. In *Engineering Applications of Large Eddy Simulations* (ed. S. A. Ragab & U. Piomelli), ASME, FED-Vol. 162, pp. 81–101.

Fureby, C. & Lofstrom, C. 1994 Large-eddy simulations of bluff body stabilized flames. In *Proc. 25th Symp. (Intl) on Combustion*, pp. 1257–1264. The Combustion Institute, Pittsburgh, PA.

Galperin, B. & Orszag, S. A. (Eds.) 1993 *Large Eddy Simulations of Complex Engineering and Geophysical Flows*. Cambridge University Press.

Gao, F. & O'Brien, E. E. 1993 A large-eddy simulation scheme for turbulent reacting flows. *Phys. Fluids* A **5**, 1282–1284.

Gardiner, C. W. 1990 *Handbook of Stochastic Methods*. Springer.

Germano, M. 1992 Turbulence: The filtering approach. *J. Fluid Mech.* **238**, 325–336.

Givi, P. 1989 Model free simulations of turbulent reactive flows. *Prog. Energy Combust. Sci.* **15**, 1–107.

Givi, P. 1994 Spectral and random vortex methods in turbulent reacting flows. In *Turbulent Reacting Flows* (ed. P. A. Libby & F. A. Williams), chap. 8, pp. 475–572. Academic.

Givi, P. & Riley, J. J. 1992 Some current issues in the analysis of reacting shear layers: Computational challenges. In *Major Research Topics in Combustion* (ed. M. Y. Hussaini, A. Kumar & R. G. Voigt), pp. 588–650. Springer.

Hussaini, M. Y., Kumar, A. & Voigt, R. G. (Eds.) 1992 *Major Research Topics in Combustion*. Springer.

Jaberi, F. A. & James, S. 1998 A dynamic similarity model for large eddy simulation of turbulent combustion. *Phys. Fluids* **10**, 1775–1777.

Jackson, T. L. 1992 A review of spatial stability analysis of compressible reacting mixing layers. In *Major Research Topics in Combustion* (ed. M. Y. Hussaini, A. Kumar & R. G. Voigt), pp. 131–161. Springer.

Jiménez, J., Liñán, A., Rogers, M. M. & Higuera, F. J. 1997 *A Priori* testing of subgrid models for chemically reacting non-premixed turbulent flows. *J. Fluid Mech.* **349**, 149–171.

Jou, W.-H. & Riley, J. J. 1989 Progress in direct numerical simulations of turbulent reacting flows. *AIAA J.* **27**, 1543–1556.

Karlin, S. & Taylor, H. M. 1981 *A Second Course in Stochastic Processes*. Academic.

Kloeden, P. E. & Platen, E. 1995 *Numerical Solution of Stochastic Differential Equations*. Applications of Mathematics, Stochastic Modelling and Applied Probability, vol. 23. Springer.

Libby, P. A. & Williams, F. A. (Eds.) 1994 *Turbulent Reacting Flows*. Academic.

Lundgren, T. S. 1969 Model equation for nonhomogeneous turbulence. *Phys. Fluids* **12**, 485–497.

Madnia, C. K. & Givi, P. 1993 Direct numerical simulation and large eddy simulation of reacting homogeneous turbulence. In *Large Eddy Simulations of Complex Engineering and Geophysical Flows* (ed. B. Galperin & S. A. Orszag), chap. 15, pp. 315–346. Cambridge University Press.

Mathey, F. & Chollet, J. P. 1997 Large eddy simulation of turbulent reactive flows. In *Proc. Eleventh Symp. on Turbulent Shear Flows*, pp. 16.19–16.24. Grenoble, France.

McMurtry, P. A., Riley, J. J. & Metcalfe, R. W. 1989 Effects of heat release on the large scale structures in a turbulent reacting mixing layer. *J. Fluid Mech.* **199**, 297–332.

McMurtry, P. A., Menon, S. & Kerstein, A. R. 1992 A linear eddy sub-grid model for turbulent reacting flows: Application to hydrogen-air combustion. In *Proc. 24th Symp. (Intl) on Combustion*, pp. 271–278. The Combustion Institute, Pittsburgh, PA.

McMurtry, P. A., Menon, S. & Kerstein, A. R. 1993 Linear eddy modeling of turbulent combustion. *Energy Fuels* **7**, 817–826.

Menon, S., McMurtry, P. A. & Kerstein, A. K. 1993 A linear eddy sugbrid model of turbulent

combustion. In *Large Eddy Simulations of Complex Engineering and Geophysical Flows* (ed. B. Galperin & S. A. Orszag), chap. 14, pp. 287–314. Cambridge University Press.

Michalke, A. 1965 On spatially growing disturbances in an inviscid shear layer. *J. Fluid Mech.* **23**, 521–544.

Miller, R. S., Madnia, C. K. & Givi, P. 1994 Structure of a turbulent reacting mixing layer. *Combust. Sci. Tech.* **99**, 1–36.

Möller, S. I., Lundgren, E. & Fureby, C. 1996 Large eddy simulations of unsteady combustion. In *Proc. 26th Symp.* (*Intl*) *on Combustion*, pp. 241. The Combustion Institute, Pittsburgh, PA.

Moser, R. D. & Rogers, M. M. 1991 Mixing transition and the cascade of small scales in a plane mixing layer. *Phys. Fluids* A **3**, 1128–1134.

Mungal, M. G. & Dimotakis, P. E. 1984 Mixing and combustion with low heat release in a turbulent mixing layer. *J. Fluid Mech.* **148**, 349–382.

O'Brien, E. E. 1980 The probability density function (PDF) approach to reacting turbulent flows. In *Turbulent Reacting Flows* (ed. P. A. Libby & F. A. Williams), chap. 5, pp. 185–218. Springer.

Paranthoen, P., Petit, C. & Lecordier, J. C. 1982 The effect of thermal prong-wire interaction on the response of a cold wire in gaseous flows (air, argon and helium). *J. Fluid Mech.* **124**, 457–473.

Poinsot, T. J. & Lele, S. K. 1992 Boundary conditions for direct simulations of compressible viscous flows. *J. Comput. Phys.* **101**, 104–129.

Pope, S. B. 1976 The probability approach to modeling of turbulent reacting flows. *Combust. Flame* **27**, 299–312.

Pope, S. B. 1985 PDF methods for turbulent reactive flows. *Prog. Energy Combust. Sci.* **11**, 119–192.

Pope, S. B. 1990 Computations of turbulent combustion: Progress and challenges. In *Proc. 23rd Symp.* (*Intl*) *on Combustion*, pp. 591–612. The Combustion Institute, Pittsburgh, PA.

Pope, S. B. 1994 Lagrangian pdf methods for turbulent flows. *Ann. Rev. Fluid Mech.* **26**, 23–63.

Pope, S. B. 1997 Mean field equations in PDF particle methods for turbulent reactive flows. *Tech. Rep.* FDA 97-06. Cornell University, Ithaca, NY.

Réveillon, J. & Vervisch, L. 1998 Subgrid-scale turbulent micromixing: Dynamic approach. *AIAA J.* **36**, 336–341.

Riley, J. J., Metcalfe, R. W. & Orszag, S. A. 1986 Direct numerical simulations of chemically reacting mixing layers. *Phys. Fluids* **29**, 406–422.

Risken, H. 1989 *The Fokker–Planck Equation, Methods of Solution and Applications*. Springer.

Rudy, D. H. & Strikwerda, J. C. 1980 Boundary conditions for subsonic compressible Navier–Stokes calculations. *J. Comput. Phys.* **36**, 327–338.

Salvetti, M. V. & Banerjee, S. 1995 A priori tests of a new dynamic subgrid-scale model for finite-difference large-eddy simulations. *Phys. Fluids* **7**, 2831–2847.

Sandham, N. D. & Reynolds, W. C. 1989 Some inlet-plane effects on the numerically simulated spatially-developing mixing layer. In *Turbulent Shear Flows 6*, pp. 441–454. Springer.

Scadron, M. D. & Warshawsky, I. 1952 Experimental determination of time constants and Nusselt numbers for bare-wire thermocouples in high-velocity air streams and analytic approximation of conduction and radiation errors. *NACA TN* 2599.

Spalding, D. B. & Stephenson, D. I. 1971 Laminar flame propagation in Hydrogen + Bromine mixtures. *Proc. R. Soc. Lond.* A **324**, 315–337.

Steinberger, C. J., Vidoni, T. J. & Givi, P. 1993 The compositional structure and the effects of exothermicity in a nonpremixed planar jet flame. *Combust. Flame* **94**, 217–232.

Tolpadi, A. K., Correa, S. M., Burrus, D. L. & Mongia, H. 1995 A Monte Carlo PDF method for the calculation of gas turbine combustor flow fields. *AIAA Paper* 95-2443.

Tolpadi, A. K., Hu, I. Z., Correa, S. M. & Burrus, D. L. 1996 Coupled Lagrangian Monte Carlo PDF-CFD computation of gas turbine combustor flowfields with finite-rate chemistry. *ASME Paper* 96-GT-205.

Vervisch, L. & Poinsot, T. 1988 Direct numerical simulation of non-premixed turbulent flames. *Ann. Rev. Fluid Mech.* **30**, 655–691.

Vreman, B., Geurts, B. & Kuerten, H. 1994 Realizability conditions for the turbulent stress tensor in large-eddy simulation. *J. Fluid Mech.* **278**, 351–362.

Wallace, A. K. 1981 Experimental investigation on the effects of chemical heat release on shear layer growth and entrainment. PhD thesis, University of Adelaide, Australia.

Williams, F. A. 1985 *Combustion Theory*, 2nd Edn. Benjamin/Cummings.